Universal and Ultrafast Quantum Computation Based on Free-Electron-Polariton Blockade

Aviv Karnieli,[1,2,3,*,†] Shai Tsesses,[4,5,†] Renwen Yu,[2] Nicholas Rivera,[6] Ady Arie,[7] Ido Kaminer,[4] and Shanhui Fan[1,2]

[1] *Department of Applied Physics, Stanford University, Stanford, California 94305, USA*

[2] *Department of Electrical Engineering, Stanford University, Stanford, California 94305, USA*

[3] *Raymond and Beverly Sackler School of Physics and Astronomy, Tel Aviv University, Ramat Aviv 69978, Tel Aviv, Israel*

[4] *Andrew and Erna Viterbi department of Electrical and Computer Engineering, Technion – Israel Institute of Technology, Haifa 32000, Israel*

[5] *Department of Physics and Research Laboratory of Electronics, Massachusetts Institute of Technology, Cambridge, Massachusetts 02139, USA*

[6] *Department of Physics, Harvard University, Cambridge, Massachusetts 02138, USA*

[7] *School of Electrical Engineering, Fleischman Faculty of Engineering, Tel Aviv University 69978, Tel Aviv, Israel*

(Received 8 March 2023; revised 1 November 2023; accepted 16 January 2024; published 6 March 2024)

Cavity QED, wherein a quantum emitter is coupled to electromagnetic cavity modes, is a powerful platform for implementing quantum sensors, memories, and networks. However, due to the fundamental trade-off between gate fidelity and execution time, as well as limited scalability, the use of cavity QED for quantum computation was overtaken by other architectures. Here, we introduce a new element into cavity QED—a free charged particle, acting as a flying qubit. Using free electrons as a specific example, we demonstrate that our approach enables ultrafast, deterministic, and universal discrete-variable quantum computation in a cavity-QED-based architecture, with potentially improved scalability. Our proposal hinges on a novel excitation blockade mechanism in a resonant interaction between a free-electron and a cavity polariton. This nonlinear interaction is faster by several orders of magnitude with respect to current photon-based cavity-QED gates, enjoys wide tunability and can demonstrate fidelities close to unity. Furthermore, our scheme is ubiquitous to any cavity nonlinearity, either due to light-matter coupling as in the Jaynes-Cummings model or due to photon-photon interactions as in a Kerr-type many-body system. In addition to promising advancements in cavity-QED quantum computation, our approach paves the way towards ultrafast and deterministic generation of highly entangled photonic graph states and is applicable to other quantum technologies involving cavity QED.

DOI: 10.1103/PRXQuantum.5.010339

I. INTRODUCTION

Quantum computation has the potential to unlock unprecedented capabilities for solving difficult problems [1], and has been the focal point of research across many physical disciplines, with several realizations thus far [2–10]. One of the earliest approaches to quantum computation relies on cavity QED [11–17]: a system in which a stationary matter qubit (such as an atom [18–22], a quantum dot [23–29], a defect center [30], or even a superconducting artificial atom [31–33]) interacts strongly with a "flying" (i.e., propagating) photonic qubit [18,34–36] via the engineering of their electromagnetic environment (e.g., via a cavity) [18,20,23,34,37–42]. Quantum computing in CQED [13,18–21,26,28,29,33,35,36,43–46] can be achieved by applying quantum gates through cavity-mediated interactions between the matter qubits [43,46], the photonic qubits [18,21], or a combination thereof [35,36,47,48].

Although CQED remains an important platform for several quantum technologies, including quantum sensing [49,50] and quantum networks [34,43,47,48,51–54], other architectures for quantum computing [2–10] are currently far more mature. One of the fundamental issues

*avivkarnieli@tauex.tau.ac.il

†These authors contributed equally.

plaguing cavity QED as a quantum computing platform is its inherent trade-off between gate fidelity and speed [44,45,55]. The better the cavity quality and emitter coherence, the more time it requires for interaction between the matter and photonic qubits [44,45,55], making fast, large bandwidth, and high-fidelity gates impractical, especially when attempting to implement cavity QED with inherently scalable platforms, such as integrated photonic circuits [24,56–58]. Scalability of cavity QED especially in a solid-state environment is also hindered by the need to fabricate a large number of indistinguishable emitters in identical cavities, which is difficult given the inherent variance in cavity resonance and emitter transitions that can hamper gate fidelities.

In this work, we propose to incorporate a new type of qubit into cavity QED—a flying charged-particle qubit, based on propagating charged quantum particles such as free electrons and ions, as shown in Fig. 1. Focusing on free electrons, we identify a mechanism for a *free-electron–polariton blockade*, which allows for the deterministic generation of a single hybrid light-matter excitation (a polariton), and its entanglement with a free electron, solely through the near-field interaction of the electron and the cavity. Using this free-electron–polariton blockade, we construct a universal set of quantum gates between polaritons for deterministic, discrete-variable quantum computation. For cavity-QED systems possessing strong enough nonlinearity, we show that these quantum gates can operate at timescales of less than a picosecond—orders of magnitude faster than the current state of the art in cavity QED, and significantly below the dissipation rate of the cavity-QED system. This ultrafast timescale is made possible

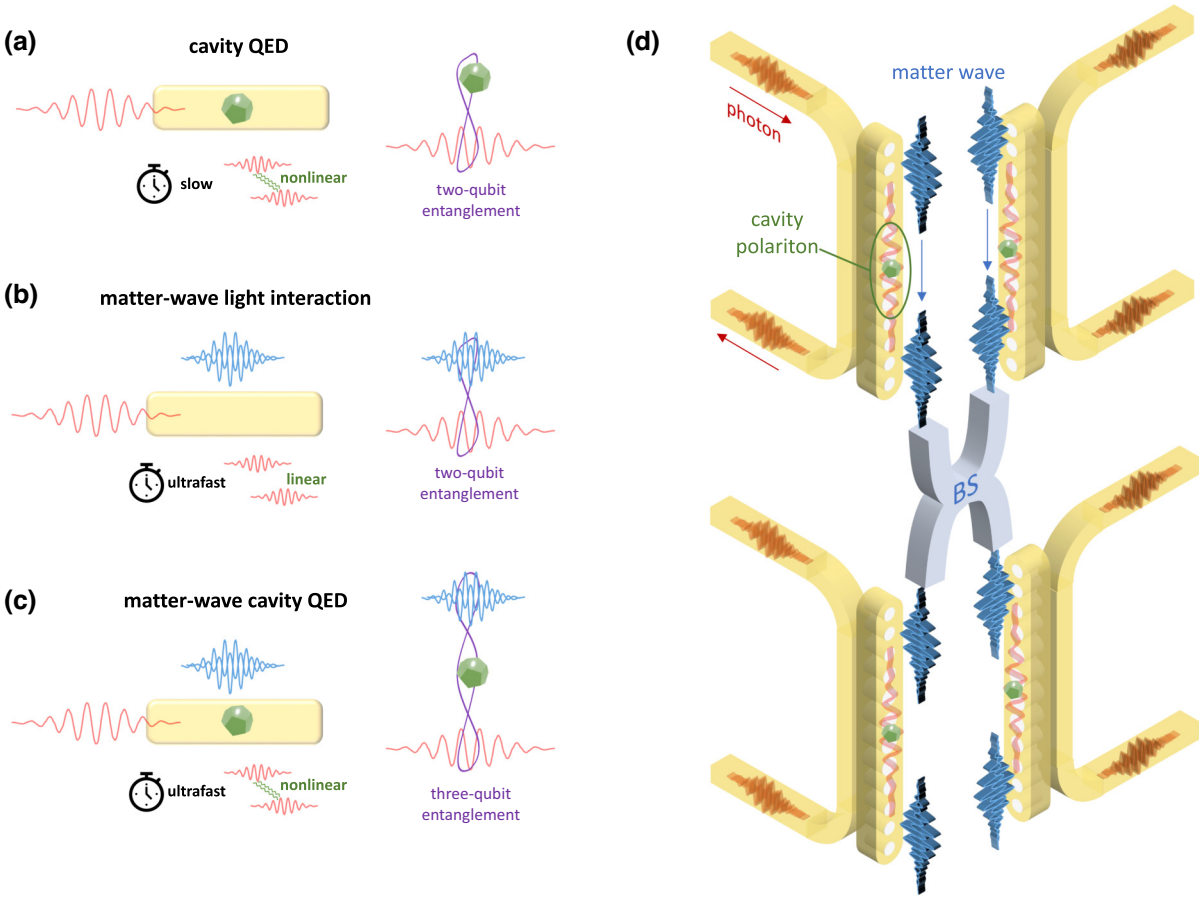

FIG. 1. Integrating flying charged-particle qubits into cavity QED. (a) In standard cavity QED, a stationary matter qubit (shown in green) interacts nonlinearly with a flying photonic qubit (red wave packet), in an interaction mediated by a cavity. Light-matter entanglement between the flying and stationary qubits is generated over slow timescales. (b) A flying charged-particle qubit (such as an electron or ion, blue wave packet) interacts linearly with a photonic qubit on an ultrafast timescale, resulting in entanglement between them. (c) When a flying charged-particle qubit drives a cavity-QED system, the light-matter interaction can be both nonlinear and ultrafast, resulting in three-qubit entanglement between the constituents of the system. (d) Concept illustration of cavity QED implemented in integrated photonic circuits and driven by a flying charged-particle qubit: ultrafast quantum gates and entanglement distribution between separate cavity polaritons is mediated by the path- and energy-encoded information of the flying charged-particle qubit (manipulated by matter wave beam splitters). Each excited cavity polariton comprises an entangled light-matter state, and its photonic part can still be used as a flying qubit, for long-distance communication between processors or over a quantum network.

owing to a resonant phase matching between the free electron and the cavity near field, and need only be longer than the nonlinearity timescale (e.g., the vacuum Rabi oscillation in the cavity). Our proposal is compatible with other cavity-QED model systems, and greatly relaxes the trade-off between gate speed and fidelity. The flying electron qubit is inherently tunable through its kinetic energy, robust to variations in cavity resonance and immune to particle loss, unlike a flying photon qubit. Thus, it can boost quantum information capacity and provide a new avenue to scale up cavity-QED-based architectures. Our scheme even facilitates the deterministic generation of highly entangled multiphoton states [59–61], and can potentially upgrade all manner of quantum technologies based on CQED, ranging from quantum sensing [62] to quantum simulation [63].

II. THEORETICAL MODEL: FREE-ELECTRON–POLARITON BLOCKADE

The quantum interaction between free electrons and light has seen dramatic advancements in the past decade, from the observation of photon-induced near-field electron microscopy [64–67] to the emerging field of free-electron quantum optics [68–79], which is fully compatible with integrated photonics [80–82]. These include demonstrations of electron-photon correlations [81,83,84], highly efficient quantum coupling between free electrons and photons [85], and theoretical proposals for continuous-variable quantum optical computation [86]. Complementarily, the quantum interaction between free electrons and quantum emitters gave rise to several theoretical investigations [87–92] focusing on the ability to infer and manipulate the emitter state.

However, we are still at the early stages of exploring the interaction of free electrons with *nonlinear* systems, which include coupling between light and matter [62,93,94] or between different light fields [95–97]. Thus, a fully quantum theoretical description of such systems is necessary, which we provide below, beginning with an intuitive explanation.

When a quantum free-electron resonantly interacts with a linear cavity, it can efficiently couple to the optical mode and spontaneously emit multiple photons [68,72,85], as illustrated in Fig. 2(a). In the course of the interaction, the electron energy becomes entangled with the generated photon number. In contrast, when a free electron is resonantly coupled to a cavity-QED-like system, it interacts with a *nonlinear* cavity possessing an inherent polariton-blockade mechanism: the existence of a first polariton in the cavity detunes the excitation of a second polariton. Hence, the free electron can only emit a single polariton, as illustrated in Fig. 2(b). The electron becomes entangled only with this single excitation, and the system therefore occupies a much smaller Hilbert space befitting discrete-variable computation.

Our model incorporates free electrons with a cavity-QED system, and captures all the effects mentioned above. The total system Hamiltonian is given by

$$H_{\mathrm{tot}} = \underbrace{H_{\mathrm{p}} + H_{\mathrm{matt}} + H_{\mathrm{e}}}_{H_0} + \underbrace{H_{\mathrm{nl}} + H_{\mathrm{ep}}}_{H_1}, \tag{1}$$

where $H_0 = H_{\mathrm{p}} + H_{\mathrm{matt}} + H_{\mathrm{e}}$ is the noninteracting part of the Hamiltonian; $H_{\mathrm{e}} = E + \int dq \hbar v q c^{\dagger}_{k_0+q} c_{k_0+q}$ is the linearized free-electron Hamiltonian under the paraxial approximation [68], with E, v, k_0 being the initial energy, velocity, and wave number of the electron, respectively, and c_k being the fermionic annihilation operator; $H_{\mathrm{p}} = \hbar\omega a^{\dagger} a$ is the photonic Hamiltonian, describing a single cavity mode with energy $\hbar\omega$ and annihilation operator a; and H_{matt} is the stationary emitter Hamiltonian, which is model dependent.

The interaction part of the Hamiltonian, $H_1 = H_{\mathrm{nl}} + H_{\mathrm{ep}}$, is comprised of the emitter-photon and electron-photon interactions, respectively. The former Hamiltonian depends on the specific cavity-QED model of choice, while the latter is given in the interaction picture, and under the nonrecoil approximation [108], by the expression

$$H_{\mathrm{ep}} = i\hbar \int dq e^{i(qv-\omega)t} \mathcal{G}_q b^{\dagger}_q a - i\hbar \int dq e^{-i(qv-\omega)t} \mathcal{G}^*_q b_q a^{\dagger}, \tag{2}$$

where q is the longitudinal recoil experienced by the free-electron; $b_q = \int dk c^{\dagger}_{k-q} c_k$ is the free-electron momentum-lowering operator by a recoil q, satisfying $[b_q, b^{\dagger}_{q'}] = 0$; and $\mathcal{G}_q = (ev/\hbar\omega) \int_0^L e^{-iqz} \mathcal{E}_z(\mathbf{r}_T, z) dz$ is the recoil-dependent coupling constant, with $e, \boldsymbol{\mathcal{E}}(\mathbf{r}_T, z), \mathbf{r}_T, L$ being the electron charge, the cavity-mode envelope, the transverse position of the electron inside the cavity near field and the cavity length, respectively. The validity of the single-mode approximation regime of the free-electron–light phase-matched interaction, and in particular, a proposal for an efficient single-mode free-electron–light interaction employing the phase-matching technique in periodic structures, is discussed in Appendix F, and illustrated in Figs. 9 and 10.

The nonlinear cavity Hamiltonian H_{nl} is generally quantified by a nonlinearity strength κ, stemming from strong coupling between light and matter. The essential difference between a nonlinear and a linear cavity is the emergence of a number-dependent energy difference between adjacent energy levels. Instead of a constant difference, i.e., $\omega_n - \omega_{n-1} = \omega$, a nonlinear cavity exhibits the relation $\omega_n - \omega_{n-1} = \omega + f(n)\kappa$, where $f(n)$ is some function of the energy-level number n. This number

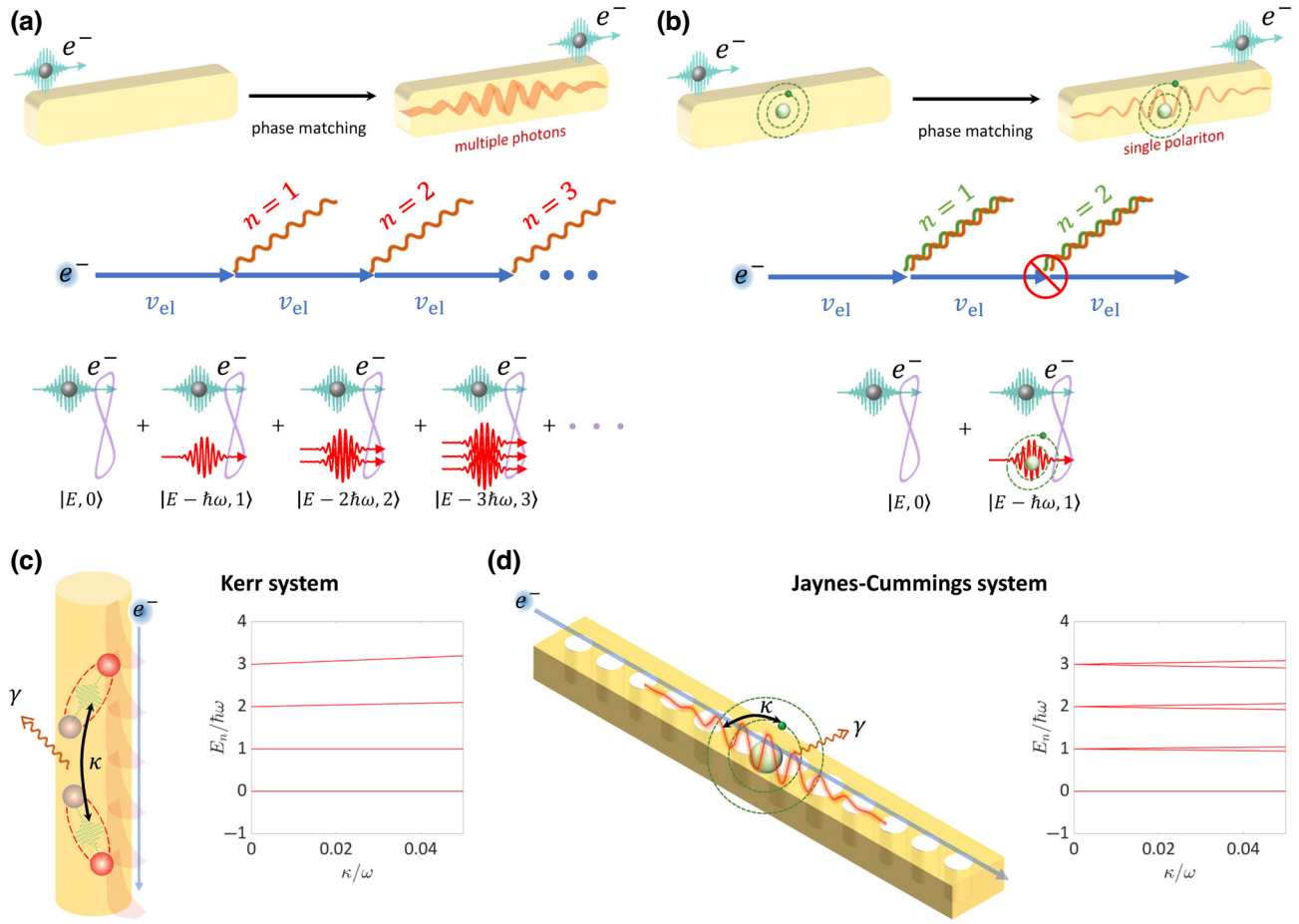

FIG. 2. Free-electron–polariton blockade. (a) A quantum free electron traverses a linear cavity while being phase matched to the cavity mode, conserving both momentum and energy. If the interaction is strong enough, the electron is able to emit multiple photons into the cavity, and its energy becomes highly entangled with the cavity photon number. (b) When the same electron traverses a cavity-QED-like system, which is comprised of a nonlinear cavity, the inherent polariton blockade effect allows for phase matching only in the process of a single polariton emission, while consecutive emission events will be phase mismatched. As a result, the electron energy becomes entangled in a minimal polariton-number Hilbert space. The dynamics then reduces to an effective two-level system driven by a quantum free electron. (c),(d) Cavity-QED models for a free-electron polariton blockade. In both settings, the electron grazes the cavity in vacuum and interacts with the polariton nearfield. The first model is a Kerr nonlinear system (c), characterized by the interaction Hamiltonian $H_{\mathrm{nl}} = \hbar\kappa a^{\dagger}a^{\dagger}aa$ and realized by interacting exciton polaritons with creation and annihilation operators $a^{\dagger}, a$ in microcavities or waveguides [98–101]. Inset: the polaritonic energy levels as a function of the nonlinearity ratio κ/ω, with spacing linearly increasing with polariton number n. The second model is a Jaynes-Cummings system (d), characterized by the interaction Hamiltonian $H_{\mathrm{nl}} = \hbar\kappa\sigma_{+}a + \hbar\kappa\sigma_{-}a^{\dagger}$ and realized, for example, by situating a two-level system with ladder operators σ_{+}, σ_{-} inside a nanobeam single-mode microcavity [23,24,102] (typical mode lengths ranging between several microns to tens of microns [103–107]), with photonic creation and annihilation operators $a^{\dagger}, a$. Inset: polaritonic energy as a function of κ/ω. While the Rabi splitting increases as $\sqrt{n}$, the spacing between adjacent energy levels decreases as $\sqrt{n} - \sqrt{n-1}$.

dependence facilitates the polariton blockade mechanism. In Appendix A, we specify two typical models for cavity-QED-like nonlinear cavity systems, determining both H_{matt} and H_{nl}: the Jaynes-Cummings (JC) model [16,17,23,24,34], considering a single two-level emitter inside a cavity; and a Kerr nonlinearity model, with inherent single-photon nonlinearity that is mediated by matter-matter interactions in a many-body system [98–101]. These two systems and their nonlinear energy spectra are depicted in Figs. 2(c) and 2(d).

In the presence of photonic losses (radiative or absorptive, with a total rate γ), which we assume to be the dominant loss mechanism in our system, the interaction-picture dynamics (subscript I) of the system density matrix, ρ_I, is given by the Lindblad master equation of the form

$$\frac{d\rho_I}{dt} = -\frac{i}{\hbar}[H_{1,I}, \rho_I] + \gamma\left(a\rho_I a^{\dagger} - \frac{1}{2}a^{\dagger}a\rho_I - \frac{1}{2}\rho_I a^{\dagger}a\right), \tag{3}$$

where $H_{1,I}$ is the interaction-picture form of $H_1 = H_{\rm nl} + H_{\rm ep}$ where $H_{\rm nl}$ depends on our model of choice [see Appendix A and Figs. 2(c) and 2(d)]. Unless stated otherwise, we will numerically integrate Eq. (3) to obtain all the results presented in this work. The details of the numerical solution are presented in Appendix C. We note that additional loss and decoherence mechanisms may be present, for example, owing to the weak interaction of the free electron with additional optical modes. In Appendix E, we provide an estimate to the maximal reduction in quantum fidelity owing to the latter effect. The quasi-single-mode approximation that we utilize in Eq. (3) and in the derivation below, assumes a considerable group-velocity mismatch between the electron and cavity modes, defining a characteristic phase-matching timescale $t_{\rm PM}$. As discussed in Appendix F, a phase-matched interaction time $t_{\rm int} = L/v$ longer than $t_{\rm PM}$ can satisfy the single-mode approximation, while still being orders of magnitude shorter than the mode lifetime γ^{-1}. In other words, the phase-matching bandwidth of the electron-photon interaction can be narrower than the cavity-free spectral range and wider than the mode linewidth, ensuring a single-mode excitation (see Fig. 9). In the limit of resonant phase matching ($L \gg 2\pi/q_0$, where q_0 is the longitudinal wave number of the cavity mode) and negligible losses ($\gamma \ll v/L$), it is possible to invoke energy and momentum conservation in the excitation of the nth energy level, such that $q = q_0$, $b_q = b_{q_0} \equiv b$, $\mathcal{G}_q = \mathcal{G}\delta(q - q_0)$ and $q_0 v = \omega_n - \omega_{n-1}$. The scattering matrix associated with the interaction thus takes an analytical closed form, which depends on the properties of the cavity.

In the linear case, it takes the well-known form of a displacement operator [68,72], i.e., $S_{\rm lin} = \exp(g_{\rm Q} b^\dagger a - g_{\rm Q}^* b a^\dagger)$, where $g_{\rm Q} = \mathcal{G}L/v$ is the dimensionless coupling constant. In contrast, the scattering matrix for the nonlinear cavity takes a distinctly different form, given by

$$S_{\rm nl} = \cos|\Omega| - i\sin|\Omega| \left(e^{i\arg\Omega} b|\bar{1}\rangle\langle\bar{0}| + e^{-i\arg\Omega} b^\dagger|\bar{0}\rangle\langle\bar{1}|\right), \tag{4}$$

where the states $|\bar{n}\rangle$, $n = 0, 1$ denote any pair of two consecutive polaritonic number states on the polariton energy ladder (detailed in the caption of Fig. 3), and Ω is the free-electron–polariton dimensionless vacuum Rabi frequency, both of which are model dependent ($\Omega = g_{\rm Q}$ or $g_{\rm Q}/\sqrt{2}$ for the Kerr and JC models, respectively; see Appendix B). Contrary to the linear case, where spontaneous emission of the electron into the cavity results in Poissonian statistics with a mean $|g_{\rm Q}|^2$, a strongly nonlinear cavity supports only a single polariton excitation, and can produce a complete population inversion between the ground state (or, in general, the lower energy state of the pair) $|\bar{0}\rangle$, and the consecutive excited state $|\bar{1}\rangle$, which we refer to as the free-electron–polariton blockade effect.

Figures 3(a) and 3(b) illustrate the continuous transition between the linear and nonlinear regimes with increasing κ, as is evidenced in both the photon statistics and the electron energy-loss spectrum (EELS) (see Appendix C for the calculation method). Figures 3(c) and 3(d), on the other hand, demonstrate the sharp dependence of the blockade effect on the phase-matching condition, whereby a blockade occurs only at the exact phase-matching condition with a specific polariton energy level. Nevertheless, the phase-matching bandwidth—being inversely proportional to the electron time of flight across the cavity, v/L—can tolerate small variations in cavity resonance (say, on the order of the cavity linewidth), which can otherwise detune a photonic flying qubit.

In a specific phase-matching condition, the blockade reduces the entire Hilbert space to that of an effective two-level system with Rabi oscillation determined by $|g_{\rm Q}|$, as shown in Fig. 4. Interestingly, tuning the electron velocity allows for selective excitation of different polaritonic transitions, which could become useful for encoding different physical qubits and for generating higher-order Fock states.

To verify that the polariton blockade can indeed be used to control the quantum state of polaritons and produce quantum gates, we calculate the fidelity $\mathcal{F} = \langle\psi|\rho|\psi\rangle$ between the state of the full system [described by the density matrix ρ in Eq. (3)], and the target pure state $|\psi\rangle$ generated by the ideal scattering matrix [Eq. (4)], for different combinations of relative loss γ/ω and coupling κ/ω. Figures 5(a) and 5(b) show the fidelity map assuming either the JC [Fig. 5(a)] or Kerr [Fig. 5(b)] model, demonstrating a clear universal behavior. Figure 5(c) presents a comparison of fidelities at the strongest coupling coefficient considered ($\kappa/\omega = 0.02$), as a function of loss ratio, where a maximal fidelity is shown to exceed 97% for both models. We emphasize that this is not a fundamental limit, as considering slower electrons [109–111], longer electron-cavity interaction length (which has been achieved experimentally [85,112]), or even multiple passes using a free-electron cavity [113], can increase the fidelity indefinitely, and can also be used to reach high-fidelity values for weaker nonlinearities. Additional decoherence mechanisms owing to the weak multimode interaction of the free electron with the cavity, and the reduction in quantum fidelity that arises from them, are discussed in Appendix E.

III. UNIVERSAL, ULTRAFAST FREE-ELECTRON-MEDIATED QUANTUM GATES

Even without a free electron present, both of the models we considered can produce quantum gates between their constituents to perform discrete-variable quantum computation, using interactions controlled and mediated by the nonlinear cavity. However, they suffer from significant limitations to gate fidelity and speed, owing to the

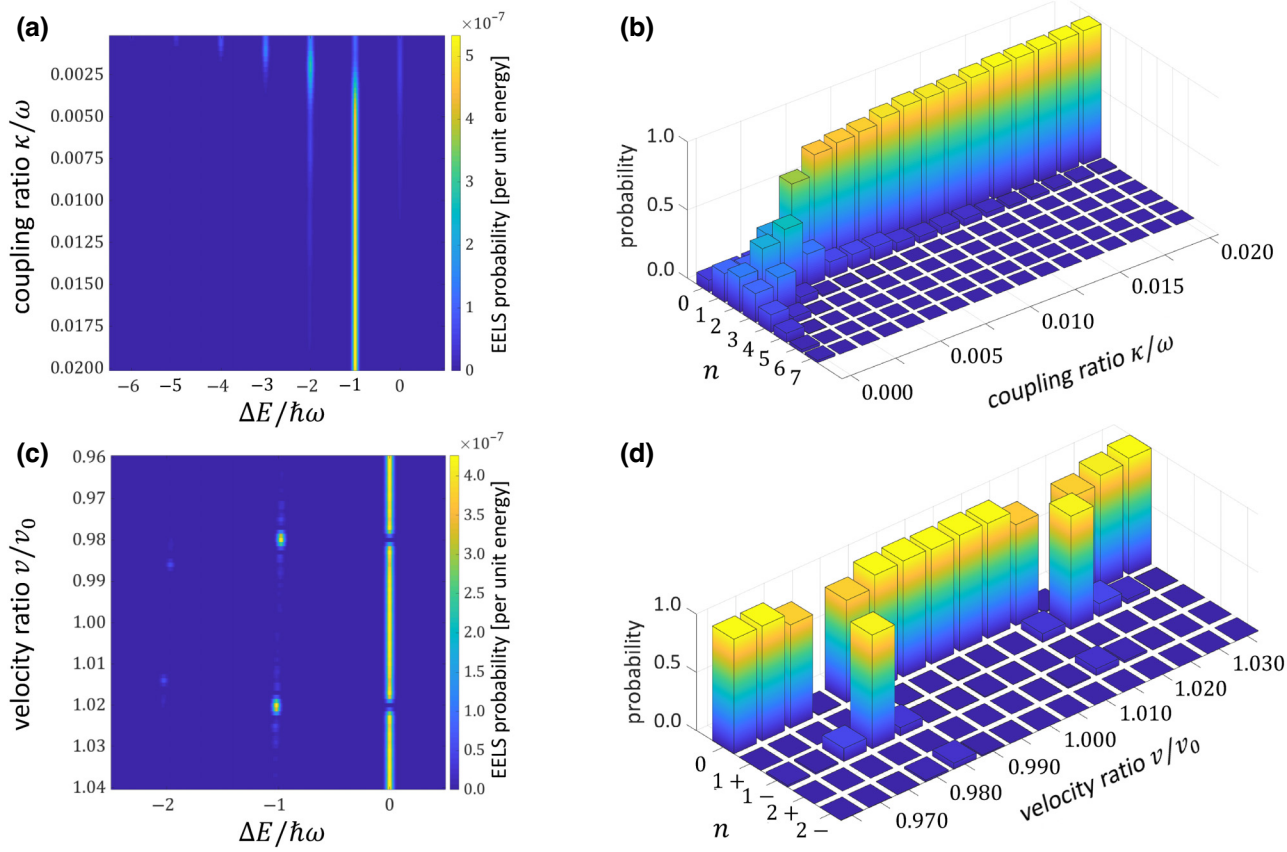

FIG. 3. Polariton statistics and electron energy-loss spectra of the free-electron–polariton blockade: dependence on cavity nonlinearity and phase-matching selectivity. Simulation results of electron energy-loss spectra (EELS) and polariton-number statistics, via the numerical integration of the Lindblad master equation [Eq. (3)]. (a),(b) Continuous transformation of the EELS (a) and photon-number statistics (b) for free-electron spontaneous emission into a Kerr nonlinear cavity as a function of the coupling ratio κ/ω. As the nonlinearity increases, complete population inversion from the Kerr-polariton ground state $|\bar{0}\rangle = |0\rangle$ and a single Kerr-polariton Fock state $|\bar{1}\rangle = |1\rangle$ occurs, whereas a Poissonian distribution is apparent in the linear case. Parameters used in the simulation are $E = 200$ keV, $L = 40$ μm, $\gamma/\omega = 10^{-5}$, $v = \omega/q_0 = 0.6953c$, $q_0 = 2\pi/532$ nm^{-1}, $g_Q = \pi/2$. (c),(d) EELS (c) and polariton-number statistics (d) for free-electron spontaneous emission into a Jaynes-Cummings nonlinear cavity as a function of the velocity ratio v/v_0 (where $v_0 = \omega/q_0 = 0.2719c$). $\kappa/\omega = 0.02$, $g_Q = \pi/\sqrt{2}$, $E = 20$ keV and all other parameters are the same as in (a),(b). In the JC example, we consider the single excitation manifold of $|\bar{0}\rangle = |0^*\rangle = |0, g\rangle$ and $|\bar{1}\rangle$, which can be either the upper ($|1+\rangle$) or lower ($|1-\rangle$) polariton state, where$|1\pm\rangle = (|g, 1\rangle \pm |e, 0\rangle)/\sqrt{2}$, with $|0\rangle, |1\rangle$ denoting the bare photon-number states and $|g\rangle(|e\rangle)$ the bare emitter ground (excited) state. Only when the free-electron velocity is tuned to phase match with a specific polariton [$v = v_\pm = (\omega \pm \kappa)/q_0 = (1 \pm 0.02)v_0$], does a full population inversion take place. In this manner, the electron velocity can be used to selectively determine the polariton type chosen for excitation. The difference in g_Q between (a),(b) and (c),(d) arises from our assumption that in the JC model, the electron couples only to the photonic degrees of freedom of the cavity.

need for large coupling efficiencies between the facilitator of the interaction (i.e., cavity) and the interacting parties (i.e., photons and/or emitter). This is not merely a technical issue, since the requirements for spectral and spatial matching between modes outside and inside the cavity impose an upper boundary to the rate at which quantum gates may be applied [44,45,55], typically on the order of 1 MHz (or once every 1 microsecond).

Therein lies the advantage of integrating electrons into these models: as an electron passes by a cavity, its interaction with the cavity persists as long as it interacts with the cavity near field. Not only does this eliminate the need for mode matching, since the electron inserts a photon into the cavity with greater ease, but it also restricts the gate application rate to the interaction time between the electron and the cavity. Considering cavities on the order of tens of microns, and fast electrons, such as can be found in transmission electron microscopes, gates can be applied within hundreds of femtoseconds (or a rate of a few THz–6 orders of magnitude in difference).

The first step towards integrating free electrons with cavity QED is to identify the physical qubits that best fit the proposed interaction mechanism. Unlike conventional cavity-QED protocols employing the JC model,

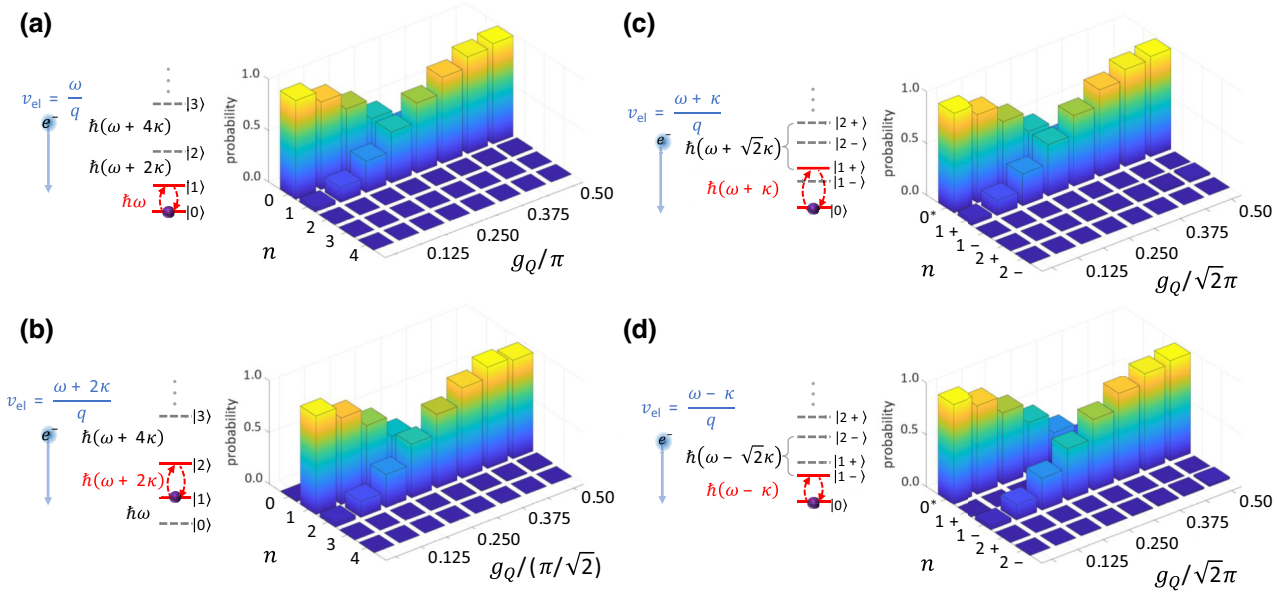

FIG. 4. Effective photonic two-level system dynamics driven by free electrons. Polariton-number statistics for both the Kerr (a),(b) and JC (c),(d) models, as a function of the dimensionless electron-light coupling g_Q. A single Rabi oscillation is apparent in all figures within a manifold preselected by the electron velocity, producing phase matching with a specific polariton transition [(a) $v = \omega/q$; (b) $v = (\omega + 2\kappa)/q$; (c) $v = (\omega + \kappa)/q$; (d) $v = (\omega - \kappa)/q$]. Each transition is illustrated in the corresponding inset nonlinear cavity energy-level diagram. Stimulated emission in the cavity produces a faster population inversion in (b), which occurs at $g_Q = \pi/\left(2\sqrt{2}\right)$. The coupling ratio κ/ω was set to 0.02 in all simulations. Otherwise, all parameters in (a),(b) and (c),(d) are the same as in Figs. 3(a),(b) and (c),(d), respectively.

wherein the emitter qubit is typically encoded in two long-lived ground states [34], here it is more natural to encode qubits in the single-excitation manifold of the polaritons (the polariton-number basis $|\bar{0}\rangle$ and $|\bar{1}\rangle$). While this encoding would be impractical for conventional cavity-QED gates in quantum memory and network applications that require long lifetimes, in our case the computation can be done orders of magnitude faster than the polariton

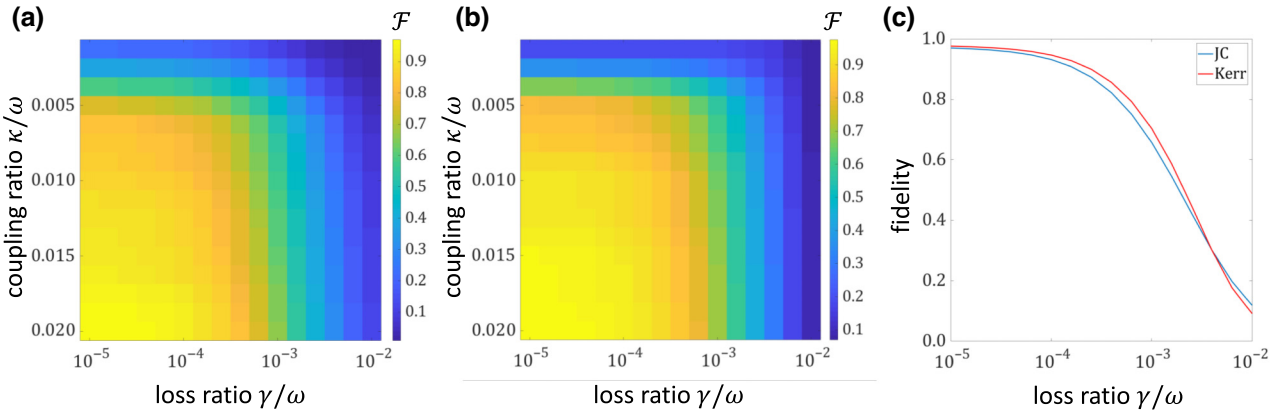

FIG. 5. Quantum state fidelity as a function of coupling strength and cavity loss. Quantum state fidelity for different photon-loss rates and coupling strengths, calculated between the total density matrix ρ_I of Eq. (3) and the target state generated by the analytic scattering matrix of Eq. (4). (a) Jaynes-Cummings cavity, with parameters $E = 20$ keV, $v = (\omega - \kappa)/q_0 = 0.2719c$, $q_0 = 2\pi/532$ nm^{-1}, $L = 40$ μm, and $g_Q = \pi/\sqrt{2}$. (b) Kerr cavity, with parameters $E = 200$ keV, $v = \omega/q_0 = 0.6953c$, $q_0 = 2\pi/532$ nm^{-1}, $L = 40$ μm, and $g_Q = \pi/2$. (c) Comparison of the polariton state fidelity in each model, for the maximal coupling $\kappa/\omega = 0.02$. Maximal fidelity for both models exceeds 97%. Apart from the cavity-loss rate, the limiting factor for the fidelities is the interplay between the cavity nonlinearity κ and the phase-matching bandwidth, proportional to v/L. If the latter is not much smaller than the former, the electron couples to higher-order polariton states that lie outside of the target Hilbert space.

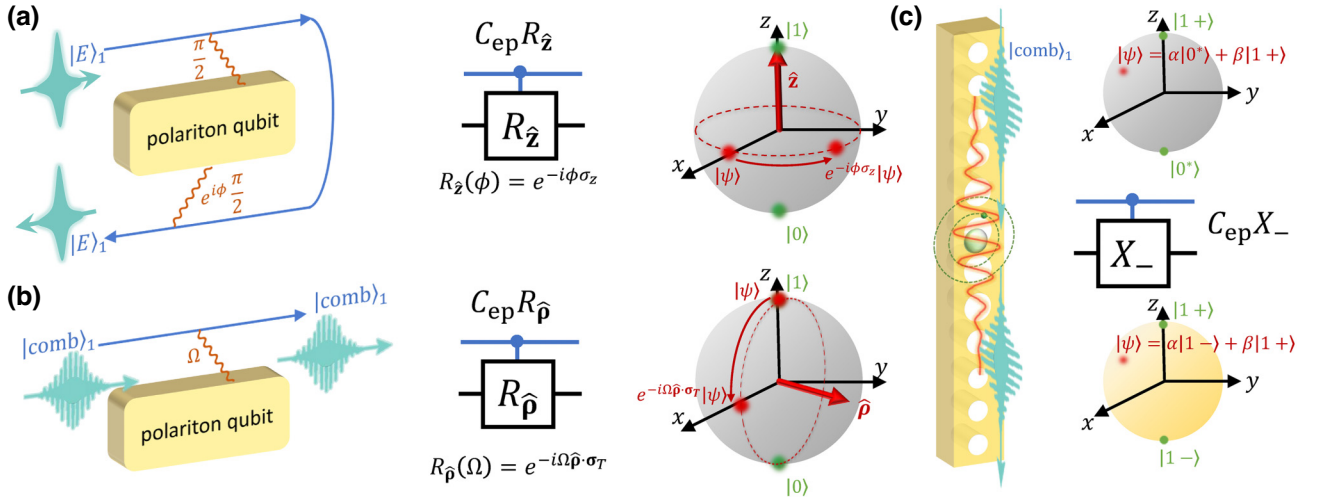

FIG. 6. Universal free-electron-driven single-qubit gates for the polariton state. (a) Electron-controlled z rotation on the polariton Bloch sphere, implemented by letting an electron interact twice with the same cavity but at different transverse locations within the nearfield. The coupling has the same magnitude $|\Omega| = \pi/2$ for each pass, yet the two paths can have a phase difference ϕ. (b) Electron-controlled transverse rotation gate about a general transverse axis $\hat{\rho} = (\cos\varphi, \sin\varphi)$ on the polariton Bloch sphere, implemented by preparing an electron in a comb state $|\mathrm{comb}(\varphi)\rangle$ and letting it interact with the cavity. (c) Transformation of the physical qubit basis from the number basis $\{|0^*\rangle, |1+\rangle\}$ (top inset) to the polariton-type basis $\{|1-\rangle, |1+\rangle\}$ (bottom inset), by applying the gate $C_{\rm ep}X_-$ with a comb electron, having a velocity tuned with the transition $|0^*\rangle \leftrightarrow |1-\rangle$.

lifetime, rendering this encoding useful for the quantum gate operations we discuss below. After the computation is performed, the tunable free-electron–polariton blockade mechanism (Fig. 4) can be employed to convert the qubit encoding from the polariton-number basis to other bases [for example, as in Fig. 6(c)], allowing for a seamless integration with conventional cavity-QED protocols.

Next, for the notion of using free-electron-mediated quantum gates in a cavity-QED-like architecture, we must demonstrate that they can support a universal set of quantum gates. Building on the analytical description of the free-electron–polariton blockade in Eq. (4), we proceed to denote the electron-cavity interaction by a single unitary operator $U(\Omega) = S_{\rm nl}$, where $S_{\rm nl}$ is the nonlinear scattering matrix of Eq. (4). We will use the unitary $U(\Omega)$ to construct a universal single-qubit gate set acting on the polariton qubit driven by a free-electron ancilla. However, as the electron energy can become entangled with the polariton state, care must be taken to make sure that the former *does not* change due to the applied gate. In other words, the free-electron energy must be *disentangled* from the polariton qubit.

First, we can describe an electron-controlled rotation by an angle ϕ about the z axis of the polariton state Bloch sphere, taking the form $C_{\rm ep}R_z(\phi) = |E\rangle_0\langle E|_0 \otimes I_{\rm p} + |E\rangle_1\langle E|_1 \otimes \exp(-i\phi\sigma_z)$, as illustrated in Fig. 6(a). Here, the electron is a path qubit denoted as $|E\rangle_m$, where $m = 0, 1$ represents an electron passing far away from the cavity ($m = 0$) or in close proximity to it ($m = 1$). If the electron interacts twice with the same cavity (using, e.g., an electron mirror [114]) but at different transverse locations (a and b) within the complex cavity near-field envelope, or with an adjustable phase delay, induced, for example, by a programmable electrostatic phase plate [115], having the same interaction strength $|\Omega_a| = |\Omega_b| = \pi/2$ and a relative phase $\phi = \arg\Omega_b - \arg\Omega_a$, the electron energy before and after interaction remains the same. The resulting polariton gate becomes

$$R_z(\phi) = \exp(-i\phi\sigma_z) = U\left(\frac{\pi}{2}e^{i\phi}\right)U\left(\frac{\pi}{2}\right) = e^{-i\phi}|\bar{0}\rangle\langle\bar{0}| + e^{i\phi}|\bar{1}\rangle\langle\bar{1}|, \tag{5}$$

where we used the fact that $bb^\dagger = b^\dagger b = 1$. Discarding a global phase, the gate $R_z(\phi)$ is the general phase gate $P(2\phi)$, and for $\phi = \pi/2, \pi/4$, and $\pi/8$, we can implement electron-controlled Z, S, and T gates, respectively.

Additionally, we describe an electron-controlled rotation by an angle $|\Omega|$ about a transverse axis $\hat{\rho} = (\cos\varphi, \sin\varphi)$ of the polariton state Bloch sphere, taking the form $C_{\rm ep}R_{\hat{\rho}}(|\Omega|) = |\mathrm{comb}(\varphi)\rangle_0\langle\mathrm{comb}(\varphi)|_0 \otimes I_{\rm p} + |\mathrm{comb}(\varphi)\rangle_1\langle\mathrm{comb}(\varphi)|_1 \otimes \exp(-i|\Omega|\hat{\rho}\cdot\sigma_T)$, as illustrated in Fig. 6(b). Here, the electron is prepared in a free-electron comb state [72] of phase φ, ideally defined as $|\mathrm{comb}(\varphi)\rangle = \sum_l e^{il\varphi}|E + l\hbar\omega_0\rangle$, manifesting as equal superpositions of electron energies in the spectral domain, or as ultrashort electron pulse trains in real space. These can be prepared using a series of laser modulations and free-space propagations [116,117]. Being eigenstates of the electron ladder operators b and $b^\dagger$, electron comb states do not get entangled with the polariton qubit, but rather induce a semiclassical drive that, in the linear regime, excites

a Glauber coherent state in the cavity [72]. In our case, applying the unitary in Eq. (4) on the state $|\mathrm{comb}(\varphi)\rangle_1$ (and assuming that $\arg\Omega = 0$ for simplicity), we find

$$\begin{aligned} R_{\hat{\rho}}(|\Omega|) &= \exp(-i|\Omega|\hat{\rho}\cdot\sigma_T) = U(|\Omega|)|\mathrm{comb}(\varphi)\rangle_1 \\ &= \left[\cos|\Omega| - i\sin|\Omega|\left(e^{i\varphi}|\bar{1}\rangle\langle\bar{0}| + e^{-i\varphi}|\bar{0}\rangle\langle\bar{1}|\right)\right] \\ &\quad \otimes |\mathrm{comb}(\varphi)\rangle_1. \end{aligned} \tag{6}$$

In this manner, we can implement elementary gates such as $\exp(-i(\pi/2)\sigma_x) = -iX$, $\exp(-i(\pi/4)\sigma_y) = HZ$ and the Hadamard gate $\exp(-i(\pi/2)\sigma_x)\exp(-i(\pi/4)\sigma_y) = -iH$. Finally, combining the two electron-controlled gates of Eqs. (5) and (6) implements a universal set of single-qubit gates, which can be readily used for state preparation and readout done exclusively by free electrons. The gate $C_{\mathrm{ep}}R_{\hat{\mathbf{x}}}$, as presented in Fig. 6(c), can serve a purpose other than performing single-qubit operations: by selectively tuning the free-electron–polariton blockade to a different polaritonic transition, it can transform a physical qubit in the polariton number basis to other bases, such as the polariton-type (upper and lower polariton) basis, or to a qubit encoding using two emitter ground states. This transformation may be important for certain cavity-QED applications such as quantum memories and quantum networks [34,43,47,48,51–54].

Now that we have established a universal single-qubit gate set, we must also present a two-qubit gate between polaritons that supports universal quantum computation, with the electron acting as an ancilla [118]. A deterministic two-polariton gate can be achieved by the interaction of an electron with two consecutive cavities, while making sure to disentangle the electron ancilla from the state of the two polariton qubits.

The first stage of a proposed two-polariton controlled-Z gate is an entanglement operation wherein the first polariton qubit controls the path of the free electron, realizing a *controlled path* (C_{pe}Path) gate, as depicted in Fig. 6(a). First, the free-electron ancilla qubit is prepared in state $|E\rangle_1$ and interacts with the first cavity with coupling $\Omega = (\pi/2)e^{i\phi}$, entangling the electron energies $|E \pm \hbar\omega\rangle_1$ with the polariton computational basis states. Next, the electron passes through an electron spectrometer, separating the two electron energies into two different paths. Finally, a second interaction with the cavity, with the same coupling $\Omega = (\pi/2)e^{i\phi}$, restores the initial electron energy E in each of the output paths. Acting on a general polariton qubit state $|\psi\rangle = \alpha|\bar{0}\rangle + \beta|\bar{1}\rangle$ and a free-electron ancilla in state $|E\rangle_1$, the C_{pe}Path gate results in

$$\begin{aligned} C_{\mathrm{pe}}\mathrm{Path}|\psi\rangle\,|E\rangle_1 &= \alpha|0\rangle|E\rangle_0 + \beta|1\rangle|E\rangle_1 \\ &= X_{\mathrm{e}}C_{\mathrm{pe}}X|\psi\rangle|E\rangle_1, \end{aligned} \tag{7}$$

where X_{e} and $C_{\mathrm{pe}}X$ denote, respectively, a NOT gate acting on the electron and a CNOT gate with polariton control qubit and electron target qubit. The equivalent circuit of C_{pe}Path is depicted in Fig. 7(a).

The next stage of the gate would be to apply a controlled-Z gate on the second polariton qubit, controlled by the free electron [the $C_{\mathrm{ep}}Z$ gate of Fig. 6(a)]. Next, a Hadamard gate H is applied on the electron qubit. The latter can be implemented, for example, using ponderomotive beam splitters [119], elastic Kapitza-Dirac diffraction from a standing wave [120], or a PINEM interaction [65], as depicted in Fig. 7(b). Finally, a second $C_{\mathrm{ep}}Z$ gate is applied, this time on the first polariton qubit. The Hadamard and second $C_{\mathrm{ep}}Z$ gate disentangle the free electron from the polariton qubits, after which the electron is found deterministically in the state $(|E\rangle_0 + |E\rangle_1)/\sqrt{2}$. A final application of a Hadamard gate transforms the ancilla state to $|E\rangle_0$. Figure 7(c) depicts the explicit and equivalent circuit of the two-polariton CZ gate (see Fig. 8 in Appendix D for derivation). Clearly, the action of the equivalent circuit is to implement a controlled-Z operation between the two bottom qubits, mediated by the top ancilla qubit.

IV. CONSIDERATIONS TOWARD AN EXPERIMENTAL REALIZATION

The demonstration of our proposed architecture for quantum computation should motivate further improvement in the performance of the state of the art in cavity-QED systems and in achieving strong free-electron–photon coupling. The most important requirement for realizing the full potential of our proposal is to find a cavity-QED system possessing a strong enough nonlinearity, which is challenging in photonic microcavity systems. The requirement for a highly efficient electron-photon interaction (g_{Q} larger than unity) is a further challenge, as our scheme requires $g_{\mathrm{Q}} > 1$, while the state of the art for all-dielectric structures is $g_{\mathrm{Q}} \sim 0.1$ [81,121]. This could be theoretically increased using optimized all-dielectric structures [82,122], or using hybrid dielectric-metal waveguides [85], for which the experimental values recently reached $g_{\mathrm{Q}} = 1$. More specifically, the high blockade fidelity sets an upper bound for the application rate of the electron-mediated quantum gates, since the blockade frequency—on the order of the cavity nonlinearity, κ—must be far greater than the free-electron phase-matching bandwidth $\Delta\omega_{\mathrm{PM}} \sim 1/T = v/L$. In turn, this relative bandwidth $\Delta\omega_{\mathrm{PM}}/\omega$ must be far greater than the relative energy uncertainties of both the electron ($\Delta E/E$) and the cavity mode (γ/ω). Thus, in general, we require

$$\frac{\gamma}{\omega}, \frac{\Delta E}{E} \ll \frac{\Delta\omega_{\mathrm{PM}}}{\omega} \ll \frac{\kappa}{\omega}. \tag{8}$$

The range of parameters currently demonstrated in experiment suggests that a proof-of-principle experiment of the free-electron polariton blockade effect can be pursued.

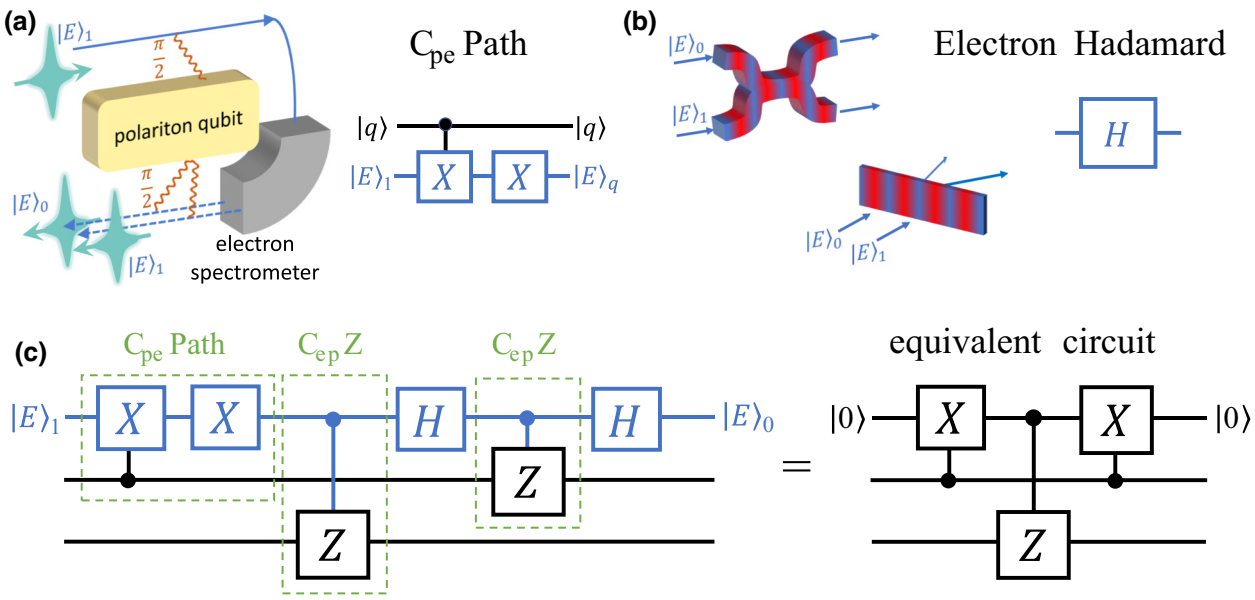

FIG. 7. Two-polariton controlled-Z gate mediated by a free electron. (a) controlled-path (C_{pe}Path) gate between a polariton control qubit and a free-electron target qubit, prepared in an initial state $|E\rangle_1$. The electron interacts with the cavity with coupling strength $\Omega = \pi/2$, either losing or gaining an amount $\hbar\omega$ of energy. Then, the electron passes through an electron spectrometer, which translates the resulting different electron energies into two different output paths, both interacting again with the same cavity, restoring the original electron energy. The result is an entangled state wherein the polariton controls the output path of the electron, with an equivalent circuit as shown in the inset. (b) A free-electron Hadamard gate (realized, for example, by a ponderomotive beam splitter, Kapitza-Dirac elastic diffraction, a PINEM interaction, etc.). (c) The quantum circuit of the two-polariton controlled-Z gate and its equivalent form. The first polariton qubit controls the free-electron ancilla by C_{pe}Path. Then, the electron drives a $C_{ep}Z$ gate acting on the second polariton qubit. The electron is disentangled from the polaritons by application of an electron Hadamard gate H followed by a second $C_{ep}Z$ acting on the first qubit, and a final Hadamrd, leaving the ancilla qubit in state $|E\rangle_0$. In the equivalent circuit (derived in Fig. 8 in Appendix D), it is clear that a controlled-Z gate is applied to the two bottom qubits, mediated by the top ancilla qubit.

In the optical domain, an efficient electron-photon coupling g_Q of unity with $\Delta\omega_{PM}/\omega = \beta\lambda/2\pi L$ of 7×10^{-4} (using the experimental parameters of Ref. [85]) has already been achieved in a hybrid dielectric-metal waveguide, though with limited polariton coherence length [85], while the state of the art in an all-dielectric structure [81] is $g_Q = 0.1$ with $\Delta\omega_{PM}/\omega = 3.6 \times 10^{-3}$, with ongoing attempts to design dielectric structures exhibiting higher efficiencies [82,122]. The typical values of $\gamma/\omega, \Delta E/E$ (between 10^{-4} to 10^{-9}, depending on quality factors and electron energies), are indeed much smaller than that, as required.

However, to fully utilize the advantage of the flying charged-particle qubit for quantum computation, significant improvements in the single-photon nonlinearity and the electron-photon coupling in all-dielectric cavities are still necessary. State-of-the-art values of κ/ω are 10^{-4} with quantum dots in dielectric microcavities [23,24,123], 10^{-3} μm^2 (per unit density) in Kerr-like propagating exciton polariton systems [99–101,124], and 10^{-8} in atomic CQED systems [34,52]. Specifically, to observe features of free-electron-polariton blockade (e.g., electron energy loss spectra deviating from a Poissonian distribution), it can be seen from Figs. 3(a) and 3(b) that relative nonlinearity values of $\kappa/\omega \sim 5 \times 10^{-3}$ could be sufficient with the parameters simulated herein. This value can even be lowered by using slower electrons, since the blockade threshold for κ/ω scales as $\Delta\omega_{PM}/\omega \propto \beta\lambda/L$ [see Eq. (8)]. Values of $\kappa/\omega \sim 10^{-3}$ could be reached by considering propagating exciton polaritons in waveguides [99–101] with densities of 1 μm^{-2} [100] or above. Another possible route to increase the cavity nonlinearity is to employ quantum dots with large dipole moments (several tens of debye, as in GaAs quantum dots [125–127]) embedded in photonic crystal nanobeam cavities [23,24], which can display ultralow mode volumes even for cavity-mode lengths of several microns [103–107,128].

Using slower electrons [109–111,129] or electron cavities [113] could support lower nonlinearity values, albeit at the cost of slower gates. On the other hand, increasing the electron-photon coupling is possible using integrated photonic cavities, based on slot waveguides [122,130], nanowires [131,132], flatband photonic modes [133], photonic crystals on nanobeams [128], and fiber Bragg gratings supporting BICs [134]. Interestingly, the stringent requirements of Eq. (8) could potentially be fulfilled in the microwave range of circuit-QED systems [135], by employing few-keV electrons and centimeter-length

transmission line resonators, operating in the ultrastrong coupling regime [136,137].

V. DISCUSSION

We proposed a new paradigm for quantum computation based on a cavity-QED-like architecture with flying charged-particle qubits mediating interactions, providing a potentially enormous increase in gate application speed. We specifically focused on free-electron flying qubits interacting with cavities hosting single-photon nonlinearities of different types (JC and Kerr), introducing a novel free-electron–polariton blockade effect. The blockade reduces the entire Hilbert space to that of an effective two-level system driven by the free electron (similarly to the on-resonance ac Stark effect [138]), establishing that it can indeed enable discrete-variable gate-based quantum computation. We then described a universal quantum gate set in cavity-QED-like architectures, enabled solely by free electrons. In Appendix G, we discuss how our proposed scheme satisfies the DiVincenzo criteria [139] for quantum computation.

Contrary to the prevalent photon-based gates, which need to operate on timescales of the order of the cavity lifetime to maintain high fidelity, free-electron–based gates can operate as fast as the time of flight $T = L/v$ of the electron, only limited by the Rabi oscillation time within the cavity, while being orders of magnitude faster than the cavity lifetime, even when slow electrons (e.g., of few-keV energies) are used. Therefore, these gates will always be fundamentally faster and more robust to errors in the cavity parameters such as detuning.

Furthermore, the electron can interact with several cavities without particle loss, unlike the photon [48,52]. Its inherent coherent energy width ΔE along with the phase-matching bandwidth of its interaction with the cavity mode can aid in tolerating small changes to the polariton resonance of different cavities (of the order of several cavity lifetimes γ, which a flying photon qubit cannot tolerate), while retaining high gate fidelities of the quantum circuit. Therefore, introducing even a single flying charged-particle qubit can aid in the speed and scalability of cavity-QED quantum computing, whereas adding more flying charged-particle qubits can increase both the dimension of the computation [140–142] and the Hilbert-space dimension of the system.

Moreover, we note that our proposal can be potentially integrated in different cavity-QED quantum computing architectures, as using the flying charged-particle qubit does not impede existing methods for producing quantum gates, only adding upon them. In fact, photon-based quantum gates are more preferable for long-range communications between quantum processors or within a quantum network [34,43,47,48,51–54], and thus the current strengths of the cavity-QED platform can still be maintained. Moreover, unlike earlier demonstrations of cavity QED with flying neutral atom qubits [143–145], the free-electron–light interaction relies on a fundamentally different mechanism [68], establishing the free charged-particle qubit as a genuinely new entity in the cavity-QED model. Unlike previous works in the literature, considering the interactions of free electrons with atomic two-level emitters [87–91], the free-electron polariton blockade relies on the free-electron–photon coupling, which can be orders of magnitude stronger than the free-electron–atom coupling [85]. Further, as the free-electron–atom interaction is not phase matched, the electron can be scattered into a continuum of final energies, making disentanglement more difficult; while the analytic closed-form solution of our model holds also in the weak-coupling regime [88,89].

The interaction of a single electron with several cavities can be used to deterministically generate large-scale photonic graph states [59–61] with high fidelities, which is one of the premier bottlenecks for photonic measurement-based quantum computation [146,147]. In the same vein, continuous-variable, fault-tolerant quantum computation can also be performed using similar systems to those considered here [86,148,149], implying that flying charged-particle qubits might also enable quantum error correction in cavity-QED-based platforms [32,148,150] as well.

Finally, we stress that the free-electron–polariton blockade effect and its consequences, as detailed in our work, can open a myriad of other applications in all manner of quantum technologies. Aside from enhancing cavity-QED-based quantum sensing [49], free electrons can act as mediators for interactions between different cavities in quantum simulations of the Jaynes-Cummings-Hubbard model [63]. Potentially, this would allow much larger hopping amplitudes, opening a route towards using CQED systems to simulate Heisenberg interaction models [151], as well as interaction Hamiltonians with controllable dimensionality, sign and symmetry through time-varying electron acceleration and deceleration between consecutive interactions.

ACKNOWLEDGMENTS

A.K. and S.T. acknowledge support by the Adams Fellowship of the Israel Academy of Sciences and Humanities. A.K. further acknowledges support by the VATAT-Quantum fellowship by the Israel Council for Higher Education; the Urbanek-Chodorow postdoctoral fellowship by the Department of Applied Physics at Stanford University; the Zuckerman STEM leadership postdoctoral program; and the Viterbi fellowship by the Technion. S.T. further acknowledges support from the Yad Hanadiv Foundation through the Rothschild fellowship and from the Israeli Council for Higher Education. S.F. and R.Y. acknowledge the support of the ACHIP Collaboration funded by the Gordon and Betty Moore Foundation (GBMF4744). A.A. acknowledges the support of the Israel Science Foundation, Grant No. 969/22. N.R. acknowledges the support of

a Junior Fellowship from the Harvard Society of Fellows. S.F. acknowledges the support of a Simons Investigator in Physics grant from the Simons Foundation (Grant No. 827065).

APPENDIX A

In this Appendix, we discuss the different interaction Hamiltonians considered in this work.

To derive the free-electron–photon interaction Hamiltonian, Eq. (2), we start from the interaction Hamiltonian in second quantization $H_{\rm ep} = \int d^3r \mathbf{j}(\mathbf{r}) \cdot \mathbf{A}(\mathbf{r})$ where $\mathbf{j}(\mathbf{r}) = (e/2m)\psi^\dagger(\mathbf{r})(-i\hbar\nabla)\psi(\mathbf{r}) + \text{h.c.}$ (for a nonrelativistic electron) or $\mathbf{j}(\mathbf{r}) = ec\Psi^\dagger(\mathbf{r})\alpha\Psi(\mathbf{r})$ (for a relativistic electron) is the electron current-density operator, with $\psi(\mathbf{r})$ or $\Psi(\mathbf{r})$ denoting the fermionic scalar and spinor position space electron annihilation operator in second quantization. Here e, m, c denote the electron charge, mass, and speed of light, respectively, α the Dirac $\boldsymbol{\alpha}$ matrix, and $\mathbf{A}(\mathbf{r}) = \sum_j (i/\omega_j)\mathcal{E}_j(\mathbf{r})a_j + \text{h.c.}$ is the vector potential, comprising modes j where $\omega_j, \mathcal{E}_j(\mathbf{r}), a_j$ are the mode resonance frequencies, electric field envelope and ladder operators, respectively. Under the approximations employed below for the electron, the nonrelativistic and relativistic cases (ignoring spin) differ [152,153] only by a Lorentz factor γ in the definition of the electron velocity $v = \hbar k/m\gamma$ where k is the electron carrier wave number. In the nonrecoil approximation, we neglect quadratic corrections to the electron energy difference $E_k - E_{k-q} \cong \hbar q v$, where q is the recoil felt by the electron upon a photon emission; in the paraxial approximation, we assume that the electron has a well-defined carrier velocity v with a slowly varying envelope, and a transverse profile $\phi_T(\mathbf{r}_T)$ that does not change during the interaction with the field. Under these approximations, the current-density operator simplifies to $\mathbf{j}(\mathbf{r}) \cong ev\psi^\dagger(\mathbf{r})\psi(\mathbf{r})$ where $\psi(\mathbf{r}) = \phi_T(\mathbf{r}_T)\int dk e^{ikz} c_k$, with c_k denoting the fermionic momentum-space annihilation operator. The current operator can then be expressed as

$$\mathbf{j}(\mathbf{r}) = ev|\phi_T(\mathbf{r}_T)|^2 \int dq e^{-iqz} \int dk c^\dagger_{k+q} c_k. \tag{A1}$$

Substituting into the interaction Hamiltonian $H_{\rm ep} = \int d^3r \mathbf{j}(\mathbf{r}) \cdot \mathbf{A}(\mathbf{r})$ we find

$$\begin{aligned} H_{\rm ep} = i\hbar \sum_j \int dq \int dk c^\dagger_{k+q} c_k \\ \times \left[\frac{ev}{\hbar\omega_j} \int d^2 r_T |\phi_T(\mathbf{r}_T)|^2 \int dz e^{-iqz} \mathcal{E}_{j,z}(\mathbf{r})\right] a_j \\ - i\hbar \sum_j \int dq \int dk c^\dagger_{k-q} c_k \\ \times \left[\frac{ev}{\hbar\omega_j} \int d^2 r_T |\phi_T(\mathbf{r}_T)|^2 \int dz e^{iqz} \mathcal{E}^*_{j,z}(\mathbf{r})\right] a^\dagger_j \end{aligned} \tag{A2}$$

Now by defining $\mathcal{G}_{q,j} \equiv (ev/\hbar\omega_j)\int d^2 r_T |\phi_T(\mathbf{r}_T)|^2 \int dz e^{-iqz} \mathcal{E}_{j,z}(\mathbf{r})$, and $b_q \equiv \int dk c^\dagger_{k-q} c_k$, $b^\dagger_q \equiv \int dk c^\dagger_{k+q} c_k$ we have

$$H_{\rm ep} = i\hbar \sum_j \int dq \mathcal{G}_{q,j} b^\dagger_q a_j - i\hbar \sum_j \int dq \mathcal{G}^*_{q,j} b_q a^\dagger_j. \tag{A3}$$

Taking the single-mode approximation for the resonantly phase-matched mode j_0, with $\mathcal{G}_q = \mathcal{G}_{q,j_0}$, $a \equiv a_{j_0}$ (justified in Appendix F), and moving to the interaction picture, we recover Eq. (2) of the main text:

$$H_{\rm ep} = i\hbar \int dq e^{i(qv-\omega)t} \mathcal{G}_q b^\dagger_q a - i\hbar \int dq e^{-i(qv-\omega)t} \mathcal{G}^*_q b_q a^\dagger. \tag{A4}$$

We now discuss the two CQED models considered in this work. The first is a Kerr-type cavity, having an intrinsic nonlinearity stemming from an effective interaction between the hybrid light-matter polaritonic eigenstates of the system. The system usually consists of an ensemble of emitters inside the optical cavity, such that the Hopfield model [16] can be invoked, effectively describing the polaritons as bosons with annihilation operator a. Usually, only the polaritons in the lower branch are considered [98], such that the noninteracting part of the Hamiltonian is simply given by a linear harmonic oscillator

$$H_{\rm p} + H_{\rm matt} = \hbar\omega a^\dagger a. \tag{A5}$$

An effective interaction between the polaritons (mediated by their matter parts) dictates a Kerr-like Hamiltonian, given as

$$H_{\rm nl} = \hbar\kappa a^\dagger a^\dagger a a, \tag{A6}$$

which could be realized, for example, by considering microcavities hosting interacting exciton polaritons [98–101], as depicted in Fig. 2(c). The system has polaritonic eigenstates $|n\rangle$ having frequencies $\omega_n = n\omega + n(n-1)\kappa$, and a frequency spacing that increases with excitation number, i.e., $\omega_n - \omega_{n-1} = \omega + 2(n-1)\kappa$.

The second model we consider is a JC-type nonlinearity [16,17,23,24,34], which results from the strong coupling between two-level emitters and optical cavity modes [16], depicted in Fig. 2(d). The noninteracting part of the system Hamiltonian is

$$H_{\rm p} + H_{\rm matt} = \hbar\omega a^\dagger a + \frac{\hbar\omega}{2}\sigma_z, \tag{A7}$$

while the interaction is dominated by the Hamiltonian

$$H_{\rm nl} = \hbar\kappa\sigma_+ a + \hbar\kappa\sigma_- a^\dagger, \tag{A8}$$

where $\sigma_-, \sigma_+, \sigma_z$ are the ladder and Pauli z operators, respectively, of the single two-level emitter embedded in

the microcavity (such as an atom, molecule, or quantum dot). The emitter is assumed to be tuned to the cavity resonance, and can be found either in its ground state $|g\rangle$ or an excited state $|e\rangle$. This has both upper and lower polaritonic eigenstates, $|n+\rangle = (|g,n\rangle + |e,n-1\rangle)/\sqrt{2}$ and $|n-\rangle = (|g,n\rangle - |e,n-1\rangle)/\sqrt{2}$, in addition to a ground state $|0^*\rangle = |g0\rangle$. The polariton excitation frequencies are, respectively, $\omega_{n\pm} = n\omega \pm \sqrt{n}\kappa$, and the frequency spacing between polaritons of the same type decreases with excitation number, i.e., $\omega_{n,\pm} - \omega_{n-1,\pm} = \omega \pm \left(\sqrt{n} - \sqrt{n-1}\right)\kappa$. Note that in the electron interaction Hamiltonian of Eq. (2), we neglected the coupling between the electron and the emitter, since it is usually much weaker [87–89].

APPENDIX B

In this Appendix, we derive the expression for the analytic form of the scattering matrix. We first exemplify the free-electron polariton blockade effect for the case of a Kerr cavity. Momentum conservation introduces a sharply peaked electron-photon coupling, taking the limiting form $\mathcal{G}_q \to \mathcal{G}\delta(q-q_0)$, which, upon performing the dq integral in Eq. (1), expanding the operators a and $a^\dagger$ in terms of the nonlinear cavity eigenstates (which for a Kerr cavity, are simply Fock states), and tuning the electron velocity such that $q_0 v - \omega = 0$ (i.e., only electrons of $q = q_0 = \omega/v$ contribute), reduces the electron-photon Hamiltonian to

$$H_{\rm ep} = \sum_{n=1}^{\infty} e^{i2(n-1)\kappa t} i\hbar\mathcal{G} b^\dagger \sqrt{n}|n-1\rangle\langle n| + \text{h.c.}, \tag{B1}$$

where $b \equiv b_{q_0}$, and where [unlike Eqs. (2) and (3)] we have considered an interaction picture wherein $H_{\rm nl}$ is part of the noninteracting Hamiltonian H_0, and $H_1 = H_{\rm ep}$. For the JC model, we write the photon-number states in terms of the JC eigenstates as $|n,g\rangle = (|n+\rangle + |n-\rangle)/\sqrt{2}$, $|0,g\rangle = |0^*\rangle$ and $|n,e\rangle = (|n+1,+\rangle - |n+1,-\rangle)/\sqrt{2}$, and again expand the photon ladder operator a in terms of these eigenstates. Tuning the electron velocity to the first upper-polariton excitation (the transition $|0^*\rangle \to |1+\rangle$) such that $q_0 v - \omega - \kappa = 0$, we find

$$\begin{aligned} H_{\rm ep} = {} & \frac{1}{\sqrt{2}} i\hbar\mathcal{G} b^\dagger \left(|0^*\rangle\langle 1+| + e^{-i2\kappa t}\frac{1}{\sqrt{2}}|0^*\rangle\langle 1-| \right) \\ & + \frac{1}{2} i\hbar\mathcal{G} b^\dagger \sum_{n=1}^{\infty} f_{n+} e^{i(f_{n-}-1)\kappa t}|n,+\rangle\langle n+1,+| \\ & + f_{n+} e^{-i(f_{n-}+1)\kappa t}|n,-\rangle\langle n+1,-| \\ & + f_{n-} e^{-i(f_{n+}+1)\kappa t}|n,+\rangle\langle n+1,-| \\ & + f_{n-} e^{i(f_{n+}-1)\kappa t}|n,-\rangle\langle n+1,+| + \text{h.c.}, \end{aligned} \tag{B2}$$

where $f_{n\pm} = \sqrt{n+1} \pm \sqrt{n}$. In the linear limit of both models, $\kappa = 0$ and all photonic excitations are perfectly tuned with the electron. When nonlinearity is present, the excitations other than the resonant transition of choice are detuned by an amount of at least 2κ (Kerr model) or $\left(2-\sqrt{2}\right)\kappa$ (JC). These transitions accumulate a dynamical phase that rapidly oscillates when $\kappa T \gg \pi$, where $T = L/v$ is the interaction time of the electron with the cavity. In this limit of strong nonlinearity, we can adopt the rotating-wave approximation by dropping these rapidly oscillating terms in the Hamiltonian, to finally obtain

$$H_{\rm ep} = i\hbar \begin{cases} \mathcal{G} b^\dagger a - \mathcal{G}^* b a^\dagger, & \text{linear} \\ \mathcal{G} b^\dagger |0\rangle\langle 1| - \mathcal{G}^* b|1\rangle\langle 0|, & \text{Kerr} \\ \dfrac{\mathcal{G}}{\sqrt{2}} b^\dagger |0^*\rangle\langle 1+| - \dfrac{\mathcal{G}^*}{\sqrt{2}} b|1+\rangle\langle 0^*|, & \text{JC} \end{cases}, \tag{B3}$$

We note that similar Hamiltonians can be obtained for any two consecutive transitions on the polariton energy ladder, with an adequate tuning of the electron velocity, as shown in Fig. 4.

The scattering matrix is in general given by $S = \mathcal{T}\exp\left[-(i/\hbar)\int_{-\infty}^{\infty} dt H_{\rm ep}(t)\right]$, where $\mathcal{T}$ stands for time ordering. As $H_{\rm ep}$ is now time independent, S can assume a closed form given by

$$S = \begin{cases} \exp(g_Q b^\dagger a - g_Q^* b a^\dagger), & \text{linear} \\ \cos|g_Q| - i\sin|g_Q|\left(e^{i\arg g_Q} b|1\rangle\langle 0| + e^{-i\arg g_Q} b^\dagger|0\rangle\langle 1|\right), & \text{Kerr} \\ \cos\dfrac{|g_Q|}{\sqrt{2}} - i\sin\dfrac{|g_Q|}{\sqrt{2}}\left(e^{i\arg g_Q} b|1+\rangle\langle 0^*| + e^{-i\arg g_Q} b^\dagger|0^*\rangle\langle 1+|\right), & \text{JC} \end{cases}, \tag{B4}$$

where $g_{\rm Q} = \mathcal{G}L/v$ is the dimensionless coupling constant. To capture the universal behavior of both CQED models, we define the polariton physical qubits $|\bar{0}\rangle$ and $|\bar{1}\rangle$ of the single-excitation manifold, and denote by $\Omega = g_{\rm Q}$ or $g_{\rm Q}/\sqrt{2}$ the electron-photon coupling in the Kerr and JC models, respectively, recovering the expression for the nonlinear scattering matrix of Eq. (4).

APPENDIX C

In this Appendix, we present the derivations of the electron energy-loss spectrum (EELS) and polariton number statistics derived from the numerically simulated density matrix of Eq. (3). The density matrix of the full system is given by

$$\rho = \begin{cases} \int dk \int dk' \sum_{n} \sum_{n'} \rho(n,k;n',k') |n,k\rangle \langle n',k'|, & \text{Kerr} \\ \int dk \int dk' \sum_{n} \sum_{n'} \sum_{s} \sum_{s'} \rho(n,s,k;n',s',k') |n,s,k\rangle \langle n',s',k'|, & \text{JC} \end{cases}, \tag{C1}$$

where k, n, s denote the electron wave vector, photon number, and atomic state ($s = e, g$), respectively. We numerically integrate Eq. (3) by representing the density matrices $\rho(n,k;n',k')$ and $\rho(n,s,k;n',s',k')$ as vectors in Liouville space, and the Lindbladian superoperator $\mathcal{L}\{\rho\} = -\frac{i}{\hbar}[H,\rho] + \gamma(a\rho a^\dagger - (1/2)a^\dagger a\rho - (1/2)\rho a^\dagger a)$ as a matrix [154]. The recoil-dependent couplings $\mathcal{G}_q$ appearing in Eq. (2) are given by their analytic form

$$\mathcal{G}_q = \frac{ev}{\hbar\omega} \int dz e^{-iqz} \mathcal{E}_z(z) = \frac{ev}{\hbar\omega} \mathcal{E}_0 L \,\mathrm{sinc}\left[(q - q_0)\frac{L}{2}\right] \tag{C2}$$

for a mode profile $\mathcal{E}_z(z) = \mathcal{E}_0 e^{iq_0 z}\mathrm{rect}(z/L)$. For convergence of the numerical calculation in reasonable time, we keep the dynamics sparse by initializing the free electron as a quasi-plane-wave mode and after the calculation we convolve the resulting electron state with the initial electron energy uncertainty ΔE, a strategy that was recently implemented to fit theory with experiment, giving excellent agreement [78,85]. The numerical integration is done over the interaction time $T = L/v$.

To obtain the EELS spectrum, we trace out the photonic (and in the JC model, also the atomic) degrees of freedom, resulting in the reduced electron density matrix $\rho_{\mathrm{el}} = \mathrm{Tr}_{\mathrm{ph,a}}\{\rho\}$. The EELS spectrum is given by the diagonal elements of ρ_{el}, expressed in terms of the total density matrix ρ as

$$p_{\mathrm{EELS}}(k) = \langle k|\,\rho_{\mathrm{el}}|k\rangle = \begin{cases} \sum_{n} \rho(n,k;n,k), & \text{Kerr} \\ \sum_{n} \sum_{s} \rho(n,s,k;n,s,k), & \text{JC} \end{cases}. \tag{C3}$$

To obtain the polariton number statistics, we apply a similar procedure, this time tracing out the electron degrees of freedom, resulting in the photon (or joint photon-atom) density matrix $\rho_{\mathrm{ph,a}} = \mathrm{Tr}_{\mathrm{el}}\rho$. The polariton number statistics is given by the diagonal elements of ρ_{ph} in the Kerr model, and by the diagonal elements of $\rho_{\mathrm{pol}} = U\rho_{\mathrm{ph,a}}U^\dagger$, where U is a unitary transformation performing a change of basis to the JC polariton eigenstates. The result in terms of the total density matrix ρ is

$$P(n) = \langle n|\rho_{\mathrm{ph}}|n\rangle = \int dk \rho(n,k;n,k), \tag{C4}$$

for the Kerr model and

$$P(n\pm) = \langle n \pm |\rho_{\mathrm{pol}}|n\pm\rangle = \sum_{ms} \sum_{m's'} U_{n\pm,ms} U^*_{m's',n\pm} \int dk \rho(m,s,k;m',s',k), \tag{C5}$$

for the JC model.

APPENDIX D

This Appendix contains a graphical derivation (Fig. 8) of the quantum circuit equivalent to the two-polariton controlled-Z interaction of Fig. 6(c).

APPENDIX E

This Appendix contains the derivation of the maximal reduction in fidelity due to the free-electron interaction with multiple optical modes in the multimode regime.

The unitary evolution operator describing the interaction in the multimode regime is given by

$$U = \mathcal{T} \exp\left[-\frac{i}{\hbar}\int H(t)dt\right], \tag{E1}$$

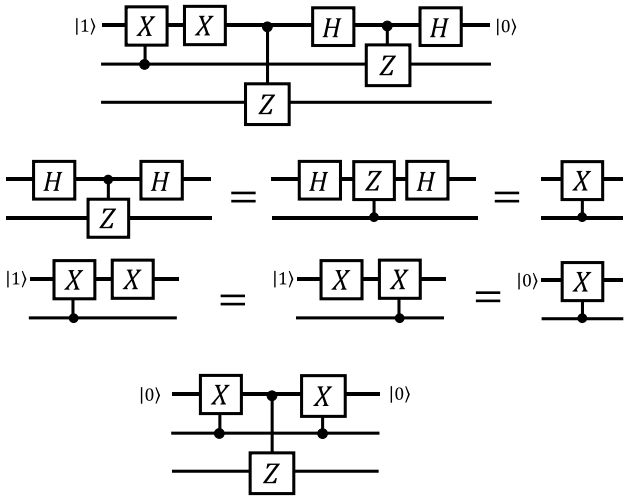

FIG. 8. Equivalent quantum circuit to the two-polariton controlled-Z gate mediated by an electron ancilla qubit.

where $\mathcal{T}$ is the time-ordering operator and $H(t) = H_{\rm sys}(t) + \sum_{j\in{\rm env}} H_{{\rm ep},j}(t)$ is the total Hamiltonian: here $H_{{\rm ep},j}$ is the electron-photon Hamiltonian with mode j of the "environment" (comprising radiating modes, other cavity modes, etc.), and $H_{\rm sys}(t)$ is the system Hamiltonian (electron-photon and emitter-photon interaction with the single cavity mode of interest). We assume that $[H_{{\rm ep},j}, H_{\rm sys}] = 0$ for every $j \in {\rm env}$, so we can separate the exponential:

$$U = \underbrace{\prod_{j\in{\rm env}} \mathcal{T}\exp\left[-\frac{i}{\hbar}\int H_{{\rm ep},j}(t)dt\right]}_{\text{electron}-\text{environment interaction}} \otimes \underbrace{\mathcal{T}\exp\left[-\frac{i}{\hbar}\int H_{\rm sys}(t)dt\right]}_{\text{electron}-\text{polariton interaction}} = U_{\rm env}\otimes U_{\rm sys}, \quad \text{(E2)}$$

Now, we can use the theory of quantum PINEM [68,72] to calculate the scattering matrices for the electron-photon interactions with the "environment" modes j, each of them is given by a displacement operator:

$$U_{\rm env} = \prod_{j\in{\rm env}} \mathcal{T}\exp\left[-\frac{i}{\hbar}\int H_{{\rm ep},j}(t)dt\right] = \prod_{j\in{\rm env}} \exp(g_{{\rm Q},j}\, b_j a_j^\dagger - g_{{\rm Q},j}^* b_j^\dagger a_j), \quad \text{(E3)}$$

where $g_{{\rm Q},j}$ is the quantum coupling to the jth mode, where $a_j, a_j^\dagger$ and $b_j, b_j^\dagger$ are the corresponding photon and electron ladder operators, respectively.

The fidelity between the target state $|\psi_{\rm sys}\rangle = U_{\rm sys}|\psi(0)\rangle$ and the state of the system coupled to the environment (initially at state $|0_j\rangle$) can be evaluated by applying $U_{\rm env}$ on $|\psi_{\rm sys}\rangle\otimes|0_j\rangle$, tracing out over all the environment modes, resulting in a mixed state $\rho_{\rm sys}$ and then calculating the fidelity via $\langle\psi_{\rm sys}|\rho_{\rm sys}|\psi_{\rm sys}\rangle$, giving

$$\mathcal{F} = \sum_{n_j} \left|\langle\psi_{\rm sys}|\langle n_j|\, U_{\rm env}|0_j\rangle|\psi_{\rm sys}\rangle\right|^2 = e^{-\sum_{j\in{\rm env}}|g_{{\rm Q},j}|^2} \sum_{n_j}\left|\langle\psi_{\rm sys}|\prod_{j\in{\rm env}}\frac{g_{{\rm Q},j}^{n_j}}{\sqrt{n_j!}} b_j^{n_j}|\psi_{\rm sys}\rangle\right|^2, \quad \text{(E4)}$$

and it is readily seen that

$$\mathcal{F} \geq e^{-\langle n_{\rm env}\rangle}, \quad \text{(E5)}$$

where $\langle n_{\rm env}\rangle = \sum_{j\in{\rm env}}|g_{{\rm Q},j}|^2$ is the parameter of a Poisson distribution, denoting the average number of photons emitted into the environment modes.

APPENDIX F

This Appendix discusses the validity of the free-electron–light single-mode regime considered in the paper, for the case of a phase-matched interaction.

We label the cavity modes by j, where j_0 is the mode jointly coupled to the material emitter and electron, and $j \neq j_0$ are other cavity modes, which may couple to the electron. Optionally, the use of a cavity incorporating a periodic structure of periodicity Λ can further mitigate momentum mismatch between the electron and the cavity mode by contributing a momentum component $2\pi/\Lambda$. For this setup, as well as for phase-matching phenomena in other fields such as in nonlinear frequency conversion [155], it is well known that the phase-matching function of the jth mode is given by

$$\Phi_j = {\rm sinc}\left(\frac{q_j v - \omega_j}{2} t_{\rm int}\right), \quad \text{(F1)}$$

where $t_{\rm int} = L/v$ is the interaction time (the time of flight of the electron of velocity v across the cavity of length L). Now, for the example of a FP cavity, $q_j = q_0 + (\pi/L)(j - j_0)$, $\omega_j = \omega_0 + v_g(\pi/L)(j - j_0)$, where v_g is the optical group velocity, and q_0 may optionally include the momentum contribution $2\pi/\Lambda$ from a periodic structure. Then we can define a second relevant timescale to the problem

$$t_{\rm PM} \equiv \frac{2}{\pi}\frac{L}{|v - v_g|}. \quad \text{(F2)}$$

Such that the phase-matching function could be written in terms of these timescales

$$\Phi_j = {\rm sinc}\left(|j - j_0|\frac{t_{\rm int}}{t_{\rm PM}}\right). \quad \text{(F3)}$$

So, in order to obtain a single-mode excitation that is still considerably shorter than the cavity lifetime γ^{-1}, the requirement on the interaction time $t_{\rm int}$ is

$$t_{\rm PM} \ll t_{\rm int} \ll \gamma^{-1}. \quad \text{(F4)}$$

Since each cavity mode j of frequency ω_j is a standing wave consisting of both positive and negative wave numbers, $\pm q_j$, the electron dispersion line $\Delta E(q)/\hbar = qv$ can intersect a given mode either in the positive-q or negative-q band. The latter condition is made possible when a periodic structure is used for phase-matching purposes, as mentioned above, to mitigate momentum mismatch between the electron and the cavity mode. Moreover, the use of periodic structures allows for creating the required large group-velocity mismatch between the electron and the photonic mode (e.g., $v_g = -v$, which could be obtained

with swift electrons, as exemplified below), as it decouples the magnitude of the photonic phase velocity from the photonic group velocity.

For intersecting a cavity mode at negative q using a periodic structure, the photon group velocity is also negative, $v_g < 0$, and the ratio between t_{int} and t_{PM} can be explicitly written as

$$\frac{t_{\text{int}}}{t_{\text{PM}}} = \frac{\pi}{2}\left(\frac{|v - v_g|}{v}\right). \tag{F5}$$

The requirement $t_{\text{int}} \gg t_{\text{PM}}$ can be achieved for $|v_g| \gg v$, but we emphasize that this is not a necessary condition. This requirement could be relaxed by considering the functional form of the phase-matching function, which vanishes when $t_{\text{int}}/t_{\text{PM}} = m\pi$, or equivalently, when

$$\beta = \frac{v}{c} = \frac{1}{2m-1}\frac{1}{n_g}, m = 1, 2, \ldots \tag{F6}$$

In other words, we can nullify the phase-matching functions Φ_j for all $j \neq j_0$ even when using swift electrons. For example, if $n_g = 1.45$ one may use 200, 15, 5, 2.5 keV, etc. electron energies to fulfill this condition, ranging from TEM down to SEM energies. This is illustrated for $v = -v_g$ in Fig. 9, and in Fig. 10 using a numerical example detailed below.

The use of a periodic structure allows for a wide tunability in the electron-photon coupling, lifting the often-limiting dependence on the material dispersion. As discussed above, it can further allow access to a single selected cavity mode as opposed to conventional phase-matching schemes [82], wherein $v_g \sim v > 0$ and a multimode excitation with effective mode number $N_{\text{eff}} \propto 1/|1 - v_g/v| > 1$ is inevitable. The state of the art for coupling using multimode phase matching to a (non-periodic) photonic cavity, as reported experimentally in Ref. [81], is $|g_{\text{Q}}| = 0.1$, wherein the theoretic maximal coupling per cavity mode j reported in that work was $|g_{\text{Q},j}| = |g_{\text{Q}}|/\sqrt{N_{\text{eff}}} = 0.03$. Another recent work achieved coupling values $|g_{\text{Q}}| \sim 0.1$ in slotted 2D photonic crystal cavities [121].

It is important to mention that the price paid with using periodic structures for phase matching is a possible reduction in the overlap between the electron wave function and the optical near field, since the electron now couples to the first Fourier order of the Bloch function associated with the optical mode. This reduction can be attributed with a modulation ratio, $M_1 = |c_1|/\sqrt{\sum_m |c_m|^2} < 1$, where c_m is the mth Fourier component of the near field. M_1 then quantifies the relative amplitude of the first Fourier order relative to the total field magnitude.

We now show that using designed cavities with confined mode volumes, one could potentially approach the

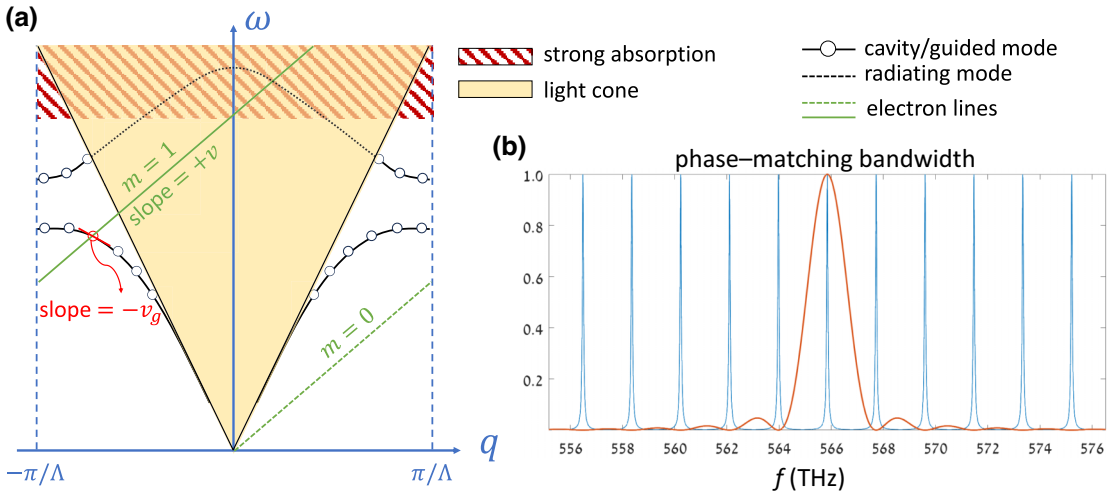

FIG. 9. Approximate single-mode interaction with periodic-structure-assisted phase-matched electron-photon coupling. (a) Illustration of phase matching to the first Fourier order of a periodic structure. The free-electron dispersion line $\Delta E/\hbar$ (in green) wraps around the Brillouin zone (BZ). Each time the line passes the right BZ edge, a new line segment continues from the left edge. The mth line segment is described by $\Delta E/\hbar = (q + 2\pi m/\Lambda)v$, for $q \in$ BZ, where v is the electron velocity and Λ the structure's period. If the mth segment intersects the photon dispersion such that $\omega(q) = (q + 2\pi m/\Lambda)v$, this corresponds to phase matching with the mth Fourier order of that periodic mode. The zeroth-line segment ($m = 0$), shown by the dashed line, does not intersect the photon dispersion anywhere in the BZ. The first-line segment ($m = 1$) intersects a guided (or cavity) mode at negative q, having a negative group velocity, as required by Eq. (F5). This line segment may also intersect radiating modes outside the material's transparency window (with a much smaller emission probability). (b) Illustration of the phase-matching bandwidth for a typical system as in (a), satisfying Eq. (F6), where only a single cavity mode is present within the phase-matching bandwidth. The parameters used for the illustration in (b) are $n_g = 2$, $E = 80$ keV, $\lambda = 532$ nm, $Q = 10^4$, $L = 40$ μm.

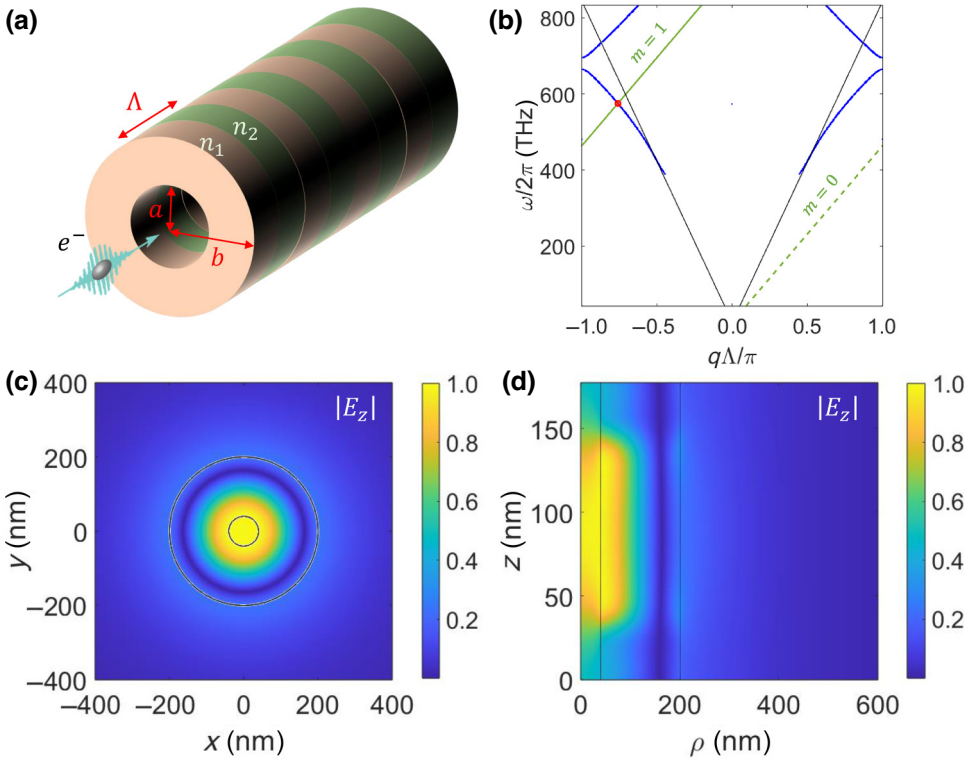

FIG. 10. Proposal for a Bragg hollow nanofiber cavity for phase-matched electron-photon coupling. (a) Illustration of the proposed structure, comprising a periodic nanofiber ($a = 40$ nm, $b = 200$ nm, $\Lambda = 177.7$ nm, $n_1 = 2.4$, e.g., as in GaN in the visible range, and $n_2 = 1.44$, as in a glass material, or using air corrugations; inside the transparency range, we assume a lossless and nondispersive material for simplicity); band structure and eigenmodes are found using a Fourier-expansion method with $N = 8$ spatial harmonics; dielectric constant profile is smoothed using a super-Gaussian function $\epsilon(z) = n_1^2 + (n_2^2 - n_1^2)\exp(-[(z - \Lambda/2)/\sigma]^p/2)$, with $\sigma = 57.7$ nm and $p = 10$). A cavity could be formed from this structure using, e.g., hollow Bragg mirrors (not shown; a different configuration, using a photonic crystal defect, is also possible). The electron (energy 100 keV, beam waist 6 nm) is passing through the hollow core. (b) Band diagram of the TM mode inside the first Brillouin zone shown in blue, light line shown in black, electron dispersion lines corresponding to the zeroth- and first-order Fourier phase matching, shown in green (higher-order phase-matching dispersion lines lie above the material transparency cutoff, which for GaN, is about 3.44 eV, or 833 THZ). Solutions to the phase-matching equation $\omega = (q + 2\pi m/\Lambda)v$ correspond to intersections between the electron dispersion and the band structure curves. Only the first-order electron dispersion line intersects the band (at $\lambda = 521.4$ nm), in the negative-q part as illustrated in Fig. 9, with $v_g = -v$ allowing for a single-mode interaction. The fact that there are no intersections between the electron dispersion for $m = 0$ (dashed line) implies that there are no TM Bloch modes whose zeroth-order Fourier component is phase matched with the electron. (c),(d) Profiles of the z component of the electric field of the TM mode: transverse profile at $z = \Lambda/2$ (c) and the longitudinal profile in the unit cell (d), with a modulation ratio $M_1 = 27\%$.

single-mode strong-coupling regime, even when considering a modulation ratio $M_1 < 1$. The geometry of an example structure is presented in Fig. 10, consisting of a hollow Bragg nanofiber, which can readily form a cavity by introducing additional hollow Bragg reflectors, or via a longitudinal defect to the photonic crystal structure. The electron passes through the hollow core. The mode considered is in the TM-mode family, which is the only mode family with a nonzero longitudinal field at the center of the hollow core (the TE, HE, and EH modes all vanish at the center, and thus have small overlap with the electron). The quantum coupling $g_{\mathrm{Q},j}$ to the single mode j with a TM field of wave number q_j is given by $g_{\mathrm{Q},j} = (e/\hbar\omega_j)\int d^3\mathbf{r}|\psi_T(\mathbf{r}_T)|^2 e^{i(\omega_j/v)z}\hat{\mathbf{z}}\cdot\mathcal{E}_{q_j}^{(\mathrm{TM})}(\mathbf{r}_T, z)$, where the TM-field envelope is $\mathcal{E}_{q_j}^{(\mathrm{TM})}(\mathbf{r}) = \sqrt{\hbar\omega_j/2\epsilon_0 V_j}\, e^{iq_j z}\mathcal{U}_{q_j}^{(\mathrm{TM})}(\mathbf{r})$, $\mathcal{U}_{q_j}^{(\mathrm{TM})}$ is the TM Bloch function, $V_j = A_j L_{\mathrm{cav}} = \int d^3\mathbf{r}\epsilon(\mathbf{r})|\mathcal{U}_{q_j}^{(\mathrm{TM})}(\mathbf{r})|^2/\max\epsilon(\mathbf{r})|\mathcal{U}_{q_j}^{(\mathrm{TM})}(\mathbf{r})|^2$ is the cavity-mode volume, A_j denotes the transverse-mode area, L_{cav} the cavity length, and $\psi_T(\mathbf{r}_T)$ the transverse electron wave function. Inside the hollow core, one can write the Bloch function as $\mathcal{U}_{q_j}^{(\mathrm{TM})}(\mathbf{r}) = \sum_m \mathcal{U}_{q_j}^{(\mathrm{TM},m)}(\mathbf{r}_T)e^{i(2\pi m/\Lambda)z}$, where $\mathcal{U}_{q_j}^{(\mathrm{TM},m)}(\mathbf{r}_T)$ is the mth Fourier component of the Bloch function.

To get better quantitative understanding, we can write the first Fourier order, single-mode coupling as $g_{\mathrm{Q},j} = I_j^{(1)}\sqrt{(\alpha/\tilde{A}_j)(L_{\mathrm{cav}}/\lambda_j)}$, where $\alpha \cong 1/137$ is the fine

structure constant, $\tilde{A}_j = A_j/\lambda_j^2$ is the mode area normalized to the free-space mode wavelength λ_j, and $I_j^{(1)} = \int d^2\mathbf{r}_T |\psi_T(\mathbf{r}_T)|^2 \hat{\mathbf{z}} \cdot \boldsymbol{u}_{qj}^{(\mathrm{TM},1)}(\mathbf{r}_T)$ is the overlap integral between the electron wave function and the z component of the first Fourier order of the Bloch function. For the proposed structure (parameters detailed in the caption of Fig. 10), a single-mode operation with $v_g = -v$ is possible, and we find that $\lambda_j = 521.4$ nm, $\tilde{A}_j = 0.2415$, $I_j^{(1)} = 0.145$ and choose $L_{\mathrm{cav}} = 10\ \mu$m, giving a single-mode coupling efficiency of $g_{\mathrm{Q},j} = 0.11$ even with a modulation ratio $M_1 = 27\%$. We believe that with a more extensive optimization, such as further reducing the mode area to a deep-subwavelength regime [128], increasing the overlap integral by pushing the field further into the hollow core vacuum [85], and increasing the modulation ratio (by working nearest to the band edge), the strong coupling regime $g_{\mathrm{Q},j} \sim 1$ could be eventually approached in a periodic dielectric structure similar to the proposed one, or using other slot-waveguide [122] or periodic waveguide [156] approaches.

APPENDIX G

In this Appendix we discuss the DiVincenzo criteria [139] and how they can be fulfilled with the proposed scheme, along with the challenges and limitations for each criterion.

1. ***A scalable physical system with a well-characterized qubit.*** We consider the cavity polariton (in the number basis, polariton-type basis, or emitter ground-state basis) as the physical qubit, and the free electron as an ancilla qubit. The scalability of our system aligns with the scalability of existing CQED schemes (and their practical limitations). However, by using flying free-electron qubits, scalability could be significantly improved: for example, the free electron can tolerate variations to the polariton resonance between different cavities, which a flying photon ancilla cannot, potentially retaining high fidelity even for complex quantum circuits. Further, a single free-electron ancilla has the potential to drive many sequential as well as parallel quantum gates.
2. ***The ability to initialize the state of the qubits to a simple fiducial state.*** Starting from the polariton ground state, any single-qubit polariton state could be prepared by consecutive interactions with free-electron ancillas.
3. ***Long relevant decoherence times.*** Gates can be applied on the timescale of hundreds of femtoseconds to several picoseconds, while the predominant decoherence time (cavity lifetime) ranges from nanoseconds to microseconds.
4. ***A universal set of quantum gates.*** We have shown the existence of a universal gate set between polaritonic qubits, mediated by free-electron ancillas, which are always disentangled from the polariton qubits at the end of the computation. We envision that the complexity of the gates could be further simplified in future work, as well as lead to other computational schemes, such as deterministic preparation of cluster states for measurement-based computation.
5. ***A qubit-specific measurement capability.*** Any measurement that can be done with conventional CQED platforms is also possible in our scheme. Moreover, such measurements can be done using the free-electron ancillas, via a single application of $U = S_{nl}(\pi/2)$ of Eq. (4) of the main text, acting on the polariton qubit and a monoenergetic electron qubit, followed by a projective measurement of the electron energy.

[1] T. D. Ladd, F. Jelezko, R. Laflamme, Y. Nakamura, C. Monroe, and J. L. O'Brien, Quantum computers, Nature **464**, 45 (2010).

[2] C. D. Bruzewicz, J. Chiaverini, R. McConnell, and J. M. Sage, Trapped-ion quantum computing: Progress and challenges, Appl. Phys. Rev. **6**, 021314 (2019).

[3] Loïc Henriet, Lucas Beguin, Adrien Signoles, Thierry Lahaye, Antoine Browaeys, Georges-Olivier Reymond, and Christophe Jurczak, Quantum computing with neutral atoms, Quantum **4**, 327 (2020).

[4] F. Arute, *et al.*, Quantum supremacy using a programmable superconducting processor, Nature **574**, 505 (2019).

[5] Nathalie P. de Leon, Kohei M. Itoh, Dohun Kim, Karan K. Mehta, Tracy E. Northup, Hanhee Paik, B. S. Palmer, N. Samarth, Sorawis Sangtawesin, and D. W. Steuerman, Materials challenges and opportunities for quantum computing hardware, Science **372**, eabb2823 (2021).

[6] H. Sen Zhong, *et al.*, Quantum computational advantage using photons, Science **370**, 1460 (2020).

[7] S. Debnath, N. M. Linke, C. Figgatt, K. A. Landsman, K. Wright, and C. Monroe, Demonstration of a small programmable quantum computer with atomic qubits, Nature **536**, 63 (2016).

[8] Lars S. Madsen, Fabian Laudenbach, Mohsen Falamarzi. Askarani, Fabien Rortais, Trevor Vincent, Jacob F. F. Bulmer, Filippo M. Miatto, Leonhard Neuhaus, Lukas G. Helt, Matthew J. Collins, Adriana E. Lita, Thomas Gerrits, Sae Woo Nam, Varun D. Vaidya, Matteo Menotti, Ish Dhand, Zachary Vernon, Nicolás Quesada, and Jonathan Lavoie, Quantum computational advantage with a programmable photonic processor, Nature **606**, 75 (2022).

[9] T. M. Graham, *et al.*, Multi-qubit entanglement and algorithms on a neutral-atom quantum computer, Nature **604**, 457 (2022).

[10] Dolev Bluvstein, Harry Levine, Giulia Semeghini, Tout T. Wang, Sepehr Ebadi, Marcin Kalinowski, Alexander Keesling, Nishad Maskara, Hannes Pichler, Markus Greiner, Vladan Vuletić, and Mikhail D. Lukin, A quantum processor based on coherent transport of entangled atom arrays, Nature **604**, 451 (2022).

[11] D. Meschede, H. Walther, and G. Müller, One-atom maser, Phys. Rev. Lett. **54**, 551 (1985).

[12] G. Rempe, H. Walther, and N. Klein, Observation of quantum collapse and revival in a one-atom maser, Phys. Rev. Lett. **58**, 353 (1987).

[13] T. Pellizzari, S. A. Gardiner, J. I. Cirac, and P. Zoller, Decoherence, continuous observation, and quantum computing: A cavity QED model, Phys. Rev. Lett. **75**, 3788 (1995).

[14] P. R. Berman, *Cavity Quantum Electrodynamics* (Academic Press, Boston, MA, 1994).

[15] H. J. Kimble, Strong interactions of single atoms and photons in cavity QED, Phys. Scr. **T76**, 127 (1998).

[16] A. Frisk Kockum, A. Miranowicz, S. De Liberato, S. Savasta, and F. Nori, Ultrastrong coupling between light and matter, Nat. Rev. Phys. **1**, 19 (2019).

[17] E. T. Jaynes and F. W. Cummings, Comparison of quantum and semiclassical radiation theories with application to the beam maser, Proc. IEEE **51**, 89 (1963).

[18] B. Hacker, S. Welte, G. Rempe, and S. Ritter, A photon–photon quantum gate based on a single atom in an optical resonator, Nature **536**, 193 (2016).

[19] J. Volz, M. Scheucher, C. Junge, and A. Rauschenbeutel, Nonlinear π phase shift for single fibre-guided photons interacting with a single resonator-enhanced atom, Nat. Photonics **8**, 965 (2014).

[20] Orel Bechler, Adrien Borne, Serge Rosenblum, Gabriel Guendelman, Ori Ezrah Mor, Moran Netser, Tal Ohana, Ziv Aqua, Niv Drucker, Ran Finkelstein, Yulia Lovsky, Rachel Bruch, Doron Gurovich, Ehud Shafir, and Barak Dayan, A passive photon–atom qubit swap operation, Nat. Phys. **14**, 996 (2018).

[21] D. Tiarks, S. Schmidt-Eberle, T. Stolz, G. Rempe, and S. Dürr, A photon–photon quantum gate based on Rydberg interactions, Nat. Phys. **15**, 124 (2018).

[22] J. D. Thompson, T. G. Tiecke, N. P. de Leon, J. Feist, A. V. Akimov, M. Gullans, A. S. Zibrov, V. Vuletić, and M. D. Lukin, Coupling a single trapped atom to a nanoscale optical cavity, Science **340**, 1202 (2013).

[23] Ryuichi Ohta, Yasutomo Ota, Masahiro Nomura, Naoto Kumagai, Satomi Ishida, Satoshi Iwamoto, and Yasuhiko Arakawa, Strong coupling between a photonic crystal nanobeam cavity and a single quantum, Appl. Phys. Lett. **98**, 173104 (2011).

[24] A. Osada, Y. Ota, R. Katsumi, M. Kakuda, S. Iwamoto, and Y. Arakawa, Strongly coupled single-quantum-dot-cavity system integrated on a CMOS-processed silicon photonic chip, Phys. Rev. Appl. **11**, 024071 (2019).

[25] J. P. Reithmaier, G. Sęk, A. Löffler, C. Hofmann, S. Kuhn, S. Reitzenstein, L. V. Keldysh, V. D. Kulakovskii, T. L. Reinecke, and A. Forchel, Strong coupling in a single quantum dot–semiconductor microcavity system, Nature **432**, 197 (2004).

[26] Ilya Fushman, Dirk Englund, Andrei Faraon, Nick Stoltz, Pierre Petroff, and Jelena Vučković, Controlled phase shifts with a single quantum, Science **320**, 769 (2008).

[27] K. Hennessy, A. Badolato, M. Winger, D. Gerace, M. Atatüre, S. Gulde, S. Fält, E. L. Hu, and A. Imamoğlu, Quantum nature of a strongly coupled single quantum dot–cavity system, Nature **445**, 896 (2007).

[28] A. Imamoglu, D. D. Awschalom, G. Burkard, D. P. DiVincenzo, D. Loss, M. Sherwin, and A. Small, Quantum information processing using quantum dot spins and cavity QED, Phys. Rev. Lett. **83**, 4204 (1999).

[29] Hanna Le Jeannic, Alexey Tiranov, Jacques Carolan, Tomás Ramos, Ying Wang, Martin Hayhurst Appel, Sven Scholz, Andreas D. Wieck, Arne Ludwig, Nir Rotenberg, Leonardo Midolo, Juan José García-Ripoll, Anders S. Sørensen, and Peter Lodahl, Dynamical photon–photon interaction mediated by a quantum emitter, Nat. Phys. **18**, 1191 (2022).

[30] M. K. Bhaskar, E. Janitz, and L. Childress, Cavity quantum electrodynamics with color centers in diamond, Optica **7**, 1232 (2020).

[31] A. Wallraff, D. I. Schuster, A. Blais, L. Frunzio, R.-S. Huang, J. Majer, S. Kumar, S. M. Girvin, and R. J. Schoelkopf, Strong coupling of a single photon to a superconducting qubit using circuit quantum electrodynamics, Nature **431**, 162 (2004).

[32] A. Blais, S. M. Girvin, and W. D. Oliver, Quantum information processing and quantum optics with circuit quantum electrodynamics, Nat. Phys. **16**, 247 (2020).

[33] A. Blais, R. S. Huang, A. Wallraff, S. M. Girvin, and R. J. Schoelkopf, Cavity quantum electrodynamics for superconducting electrical circuits: An architecture for quantum computation, Phys. Rev. A **69**, 062320 (2004).

[34] A. Reiserer and G. Rempe, Cavity-based quantum networks with single atoms and optical photons, Rev. Mod. Phys. **87**, 1379 (2015).

[35] T. Wilk, S. C. Webster, A. Kuhn, and G. Rempe, Single-atom single-photon quantum interface, Science **317**, 488 (2007).

[36] A. Reiserer, N. Kalb, G. Rempe, and S. Ritter, A quantum gate between a flying optical photon and a single trapped atom, Nature **508**, 237 (2014).

[37] A. Asenjo-Garcia, M. Moreno-Cardoner, A. Albrecht, H. J. Kimble, and D. E. Chang, Exponential improvement in photon storage fidelities using subradiance & 'selective radiance' in atomic arrays, Phys. Rev. X **7**, 031024 (2017).

[38] S. Sun, H. Kim, Z. Luo, G. S. Solomon, and E. Waks, A single-photon switch and transistor enabled by a solid-state quantum memory, Science **361**, 57 (2018).

[39] Dirk Englund, Andrei Faraon, Ilya Fushman, Nick Stoltz, Pierre Petroff, and Jelena Vučković, Controlling cavity reflectivity with a single quantum, Nature **450**, 857 (2007).

[40] Dirk Englund, Brendan Shields, Kelley Rivoire, Fariba Hatami, Jelena Vučković, Hongkun Park, and Mikhail D. Lukin, Deterministic coupling of a single nitrogen vacancy center to a photonic crystal cavity, Nano Lett. **10**, 3922 (2010).

[41] D. E. Chang, L. Jiang, A. V. Gorshkov, and H. J. Kimble, Cavity QED with atomic mirrors, New J. Phys. **14**, 063003 (2012).

[42] D. E. Chang, V. Vuletić, and M. D. Lukin, Quantum nonlinear optics — photon by photon, Nat. Photonics **8**, 685 (2014).
[43] Severin Daiss, Stefan Langenfeld, Stephan Welte, Emanuele Distante, Philip Thomas, Lukas Hartung, Olivier Morin, and Gerhard Rempe, A quantum-logic gate between distant quantum-network modules, Science **371**, 614 (2021).
[44] R. Asaoka, Y. Tokunaga, R. Kanamoto, H. Goto, and T. Aoki, Requirements for fault-tolerant quantum computation with cavity-QED-based atom-atom gates mediated by a photon with a finite pulse length, Phys. Rev. A **104**, 043702 (2021).
[45] L. M. Duan and H. J. Kimble, Scalable photonic quantum computation through cavity-assisted interactions, Phys. Rev. Lett. **92**, 127902 (2004).
[46] S. B. Zheng and G. C. Guo, Efficient scheme for two-atom entanglement and quantum information processing in cavity QED, Phys. Rev. Lett. **85**, 2392 (2000).
[47] A. D. Boozer, A. Boca, R. Miller, T. E. Northup, and H. J. Kimble, Reversible state transfer between light and a single trapped atom, Phys. Rev. Lett. **98**, 193601 (2007).
[48] Stephan Ritter, Christian Nölleke, Carolin Hahn, Andreas Reiserer, Andreas Neuzner, Manuel Uphoff, Martin Mücke, Eden Figueroa, Joerg Bochmann, and Gerhard Rempe, An elementary quantum network of single atoms in optical cavities, Nature **484**, 195 (2012).
[49] C. L. Degen, F. Reinhard, and P. Cappellaro, Quantum sensing, Rev. Mod. Phys. **89**, 035002 (2017).
[50] A. Reiserer, S. Ritter, and G. Rempe, Nondestructive detection of an optical photon, Science **342**, 1349 (2013).
[51] Holger P. Specht, Christian Nölleke, Andreas Reiserer, Manuel Uphoff, Eden Figueroa, Stephan Ritter, and Gerhard Rempe, A single-atom quantum memory, Nature **473**, 190 (2011).
[52] A. Reiserer, Cavity-enhanced quantum network nodes, Rev. Mod. Phys. **94**, 041003 (2022).
[53] H. J. Briegel, W. Dür, J. I. Cirac, and P. Zoller, Quantum repeaters: The role of imperfect local operations in quantum communication, Phys. Rev. Lett. **81**, 5932 (1998).
[54] Sreraman Muralidharan, Linshu Li, Jungsang Kim, Norbert Lütkenhaus, Mikhail D. Lukin, and Liang Jiang, Optimal architectures for long distance quantum communication, Sci. Rep. **6**, 1 (2016).
[55] N. Kalb, A. Reiserer, S. Ritter, and G. Rempe, Heralded storage of a photonic quantum bit in a single atom, Phys. Rev. Lett. **114**, 220501 (2015).
[56] B. Bartlett and S. Fan, Universal programmable photonic architecture for quantum information processing, Phys. Rev. A **101**, 042319 (2020).
[57] B. Bartlett, B. Bartlett, B. Bartlett, A. Dutt, and S. Fan, Deterministic photonic quantum computation in a synthetic time dimension, Optica **8**, 1515 (2021).
[58] J. Wang, F. Sciarrino, A. Laing, and M. G. Thompson, Integrated photonic quantum technologies, Nat. Photonics **14**, 273 (2019).
[59] P. Thomas, L. Ruscio, O. Morin, and G. Rempe, Efficient generation of entangled multiphoton graph states from a single atom, Nature **608**, 677 (2022).
[60] D. Cogan, Z.-E. Su, O. Kenneth, and D. Gershoni, Deterministic generation of indistinguishable photons in a cluster state, Nat. Photonics **2023**, 1 (2023).
[61] I. Schwartz, D. Cogan, E. R. Schmidgall, Y. Don, L. Gantz, O. Kenneth, N. H. Lindner, and D. Gershoni, Deterministic generation of a cluster state of entangled photons, Science **354**, 434 (2016).
[62] Aviv Karnieli, Shai Tsesses, Renwen Yu, Nicholas Rivera, Zhexin Zhao, Ady Arie, Shanhui Fan, and Ido Kaminer, Quantum sensing of strongly coupled light-matter systems using free electrons, Sci. Adv. **9**, eadd2349 (2023).
[63] C. Noh and D. G. Angelakis, Quantum simulations and many-body physics with light, Rep. Prog. Phys. **80**, 016401 (2016).
[64] B. Barwick, D. J. Flannigan, and A. H. Zewail, Photon-induced near-field electron microscopy, Nature **462**, 902 (2009).
[65] Armin Feist, Katharina E. Echternkamp, Jakob Schauss, Sergey V. Yalunin, Sascha Schäfer, and Claus Ropers, Quantum coherent optical phase modulation in an ultrafast transmission electron microscope, Nature **521**, 200 (2015).
[66] Kangpeng Wang, Raphael Dahan, Michael Shentcis, Yaron Kauffmann, Adi Ben Hayun, Ori Reinhardt, Shai Tsesses, and Ido Kaminer, Coherent interaction between free electrons and a photonic cavity, Nature **582**, 50 (2020).
[67] Ofer Kfir, Hugo Lourenço-Martins, Gero Storeck, Murat Sivis, Tyler R. Harvey, Tobias J. Kippenberg, Armin Feist, and Claus Ropers, Controlling free electrons with optical whispering-gallery modes, Nature **582**, 46 (2020).
[68] O. Kfir, Entanglements of Electrons and Cavity Photons in the Strong-Coupling Regime, Phys. Rev. Lett. **123**, 103602 (2019).
[69] V. Di Giulio, M. Kociak, and F. J. G. de Abajo, Probing quantum optical excitations with fast electrons, Optica **6**, 1524 (2019).
[70] A. Polman, M. Kociak, and F. J. García de Abajo, Electron-beam spectroscopy for nanophotonics, Nat. Mater. **18**, 1158 (2019).
[71] M. Taleb, M. Hentschel, K. Rossnagel, H. Giessen, and N. Talebi, Phase-locked photon–electron interaction without a laser, Nat. Phys. **2023**, 1 (2023).
[72] A. Ben Hayun, O. Reinhardt, J. Nemirovsky, A. Karnieli, N. Rivera, and I. Kaminer, Shaping quantum photonic states using free electrons, Sci. Adv. **7**, 4270 (2021).
[73] Alexey Gorlach, Aviv Karnieli, Raphael Dahan, Eliahu Cohen, Avi Pe'er, and Ido Kaminer, Ultrafast nondestructive measurement of the quantum state of light using free electrons, arXiv:2012.12069 (2020).
[74] Joshua Christopher, Masoud Taleb, Achyut Maity, Mario Hentschel, Harald Giessen, and Nahid Talebi, Electron-driven photon sources for correlative electron-photon spectroscopy with electron microscopes, Nanophotonics **9**, 4381 (2020).
[75] Charles Roques-Carmes, Steven E. Kooi, Yi Yang, Nicholas Rivera, Phillip D. Keathley, John D. Joannopoulos, Steven G. Johnson, Ido Kaminer, Karl K. Berggren, and Marin Soljačić, Free-electron–light interactions in nanophotonics, Appl. Phys. Rev. **10**, 011303 (2023).

[76] X. Bendaña, A. Polman, and F. J. García De Abajo, Single-photon generation by electron beams, Nano Lett. **11**, 5099 (2011).
[77] V. Di Giulio and F. J. García De Abajo, Optical-cavity mode squeezing by free electrons, Nanophotonics **11**, 4659 (2022).
[78] Raphael Dahan, Alexey Gorlach, Urs Haeusler, Aviv Karnieli, Ori Eyal, Peyman Yousefi, Mordechai Segev, Ady Arie, Gadi Eisenstein, Peter Hommelhoff, and Ido Kaminer, Imprinting the quantum statistics of photons on free electrons, Science **373**, eabj7128 (2021).
[79] F. J. García de Abajo and V. Di Giulio, Optical exitations with electron beams: Challenges and opportunities, ACS Photonics **17**, 36 (2021).
[80] Jan-Wilke Henke, Arslan Sajid Raja, Armin Feist, Guanhao Huang, Germaine Arend, Yujia Yang, F. Jasmin Kappert, Rui Ning Wang, Marcel Möller, Jiahe Pan, Junqiu Liu, Ofer Kfir, Claus Ropers, and Tobias J. Kippenberg, Integrated photonics enables continuous-beam electron phase modulation, Nature **600**, 653 (2021).
[81] Armin Feist, Guanhao Huang, Germaine Arend, Yujia Yang, Jan-Wilke Henke, Arslan Sajid Raja, F. Jasmin Kappert, Rui Ning Wang, Hugo Lourenço-Martins, Zheru Qiu, Junqiu Liu, Ofer Kfir, Tobias J. Kippenberg, and Claus Ropers, Cavity-mediated electron-photon pairs, Science **377**, 777 (2022).
[82] G. Huang, N. J. Engelsen, O. Kfir, C. Ropers, and T. J. Kippenberg, Electron-photon quantum state heralding using photonic integrated circuits, PRX Quantum **4**, 020351 (2023).
[83] Nadezda Varkentina, Yves Auad, Steffi Y. Woo, Alberto Zobelli, Laura Bocher, Jean-Denis Blazit, Xiaoyan Li, Marcel Tencé, Kenji Watanabe, Takashi Taniguchi, Odile Stéphan, Mathieu Kociak, and Luiz H. G. Tizei, Cathodoluminescence excitation spectroscopy: Nanoscale imaging of excitation pathways, Sci. Adv. **8**, 4947 (2022).
[84] A. Konečná, F. Iyikanat, and F. J. G. de Abajo, Entangling free electrons and optical excitations, Sci. Adv. **8**, 7853 (2022).
[85] Yuval Adiv, Hao Hu, Shai Tsesses, Raphael Dahan, Kangpeng Wang, Yaniv Kurman, and Hongsheng Alexey Gorlach, Observation of 2D Cherenkov radiation, Phys. Rev. X **13**, 011002 (2023).
[86] Raphael Dahan, Gefen Baranes, Alexey Gorlach, Ron Ruimy, Nicholas Rivera, and Ido Kaminer, Creation of optical cat and GKP states using shaped free electrons, Phys. Rev. X **13**, 031001 (2023).
[87] A. Gover and A. Yariv, Free-electron-bound-electron resonant interaction, Phys. Rev. Lett. **124**, 064801 (2020).
[88] R. Ruimy, A. Gorlach, C. Mechel, N. Rivera, and I. Kaminer, Toward atomic-resolution quantum measurements with coherently shaped free electrons, Phys. Rev. Lett. **126**, 233403 (2021).
[89] Z. Zhao, X. Q. Sun, and S. Fan, Quantum entanglement and modulation enhancement of free-electron-bound-electron interaction, Phys. Rev. Lett. **126**, 233402 (2021).
[90] Bin Zhang, Du Ran, Reuven Ianconescu, Aharon Friedman, Jacob Scheuer, Amnon Yariv, and Avraham Gover, Quantum state interrogation using a preshaped free electron wavefunction, Phys. Rev. Res. **4**, 033071 (2022).
[91] Bin Zhang, Du Ran, Reuven Ianconescu, Aharon Friedman, Jacob Scheuer, Amnon Yariv, and Avraham Gover, Quantum wave-particle duality in free-electron-bound-electron interaction, Phys. Rev. Lett. **126**, 244801 (2021).
[92] D. Rätzel, D. Hartley, O. Schwartz, and P. Haslinger, Controlling quantum systems with modulated electron beams, Phys. Rev. Res. **3**, 023247 (2021).
[93] E. Arqué López, V. Di Giulio, and F. J. García De Abajo, Atomic Floquet physics revealed by free electrons, Phys. Rev. Res. **4**, 013241 (2022).
[94] J. Lim, S. Kumar, Y. S. Ang, L. K. Ang, and L. J. Wong, Quantum interference between fundamentally different processes is enabled by shaped input wavefunctions, Adv. Sci. **10**, 2205750 (2023).
[95] J. D. Cox and F. J. García De Abajo, Nonlinear interactions between free electrons and nanographenes, Nano Lett. **20**, 4792 (2020).
[96] A. Konečná, V. Di Giulio, V. Mkhitaryan, C. Ropers, and F. J. García De Abajo, Nanoscale nonlinear spectroscopy with electron beams, ACS Photonics **7**, 1290 (2020).
[97] Yujia Yang, Jan-Wilke Henke, Arslan S. Raja, F. Jasmin Kappert, Guanhao Huang, Germaine Arend, Zheru Qiu, Armin Feist, Rui Ning Wang, Aleksandr Tusnin, Alexey Tikan, Claus Ropers, and Tobias J. Kippenberg, Free-electron interaction with nonlinear optical states in microresonators, Science **383**, 168 (2024).
[98] Aymeric Delteil, Thomas Fink, Anne Schade, Sven Höfling, Christian Schneider, and Ataç İmamoğlu, Towards polariton blockade of confined exciton–polaritons, Nat. Mater. **18**, 219 (2019).
[99] D. Liran, I. Rosenberg, K. West, L. Pfeiffer, and R. Rapaport, Fully guided electrically controlled exciton polaritons, ACS Photonics **5**, 4249 (2018).
[100] Itamar Rosenberg, Dror Liran, Yotam Mazuz-Harpaz, Kenneth West, Loren Pfeiffer, and Ronen Rapaport, Strongly interacting dipolar-polaritons, Sci. Adv. **4**, eaat8880 (2018).
[101] D G Suárez-Forero, F. Riminucci, V. Ardizzone, N. Karpowicz, E. Maggiolini, G. Macorini, G. Lerario, F. Todisco, M. De Giorgi, L. Dominici, D. Ballarini, G. Gigli, A S Lanotte, K. West, K. Baldwin, L. Pfeiffer, and D. Sanvitto, Enhancement of parametric effects in polariton waveguides induced by dipolar interactions, Phys. Rev. Lett. **126**, 137401 (2021).
[102] B. J. M. Hausmann, B. J. Shields, Q. Quan, Y. Chu, N. P. de Leon, R. Evans, M. J. Burek, A. S. Zibrov, M. Markham, D. J. Twitchen, H. Park, M. D. Lukin, and M. Loncąr, Coupling of NV centers to photonic crystal nanobeams in diamond, Nano Lett. **13**, 5791 (2013).
[103] X. Li, X. Liu, Y. Qin, D. Yang, and Y. Ji, Ultra-low index-contrast polymeric photonic crystal nanobeam electro-optic modulator, IEEE Photonics J. **12**, 1 (2020).
[104] J. D. Ryckman and S. M. Weiss, Low mode volume slotted photonic crystal single nanobeam cavity, Appl. Phys. Lett. **101**, 71104 (2012).
[105] H. Choi, M. Heuck, and D. Englund, Self-similar nanocavity design with ultrasmall mode volume for

single-photon nonlinearities, Phys. Rev. Lett. **118**, 223605 (2017).
[106] Qimin Quan and Marko Loncar, Deterministic design of wavelength scale, ultra-high Q photonic crystal nanobeam cavities, Opt. Express **19**, 18529 (2011).
[107] S. Mouradian, N. H. Wan, T. Schröder, and D. Englund, Rectangular photonic crystal nanobeam cavities in bulk diamond, Appl. Phys. Lett. **111**, 21103 (2017).
[108] F. J. García de Abajo, Optical excitations in electron microscopy, Rev. Mod. Phys. **82**, 209 (2010).
[109] Aviram Massuda, Charles Roques-Carmes, Yujia Yang, Steven E. Kooi, Yi Yang, Chitraang Murdia, Karl K. Berggren, Ido Kaminer, and Marin Soljačić, Smith-Purcell radiation from low-energy electrons, ACS Photonics **5**, 3513 (2018).
[110] Fang Liu, Long Xiao, Yu Ye, Mengxuan Wang, Kaiyu Cui, Xue Feng, Wei Zhang, and Yidong Huang, Integrated Cherenkov radiation emitter eliminating the electron velocity threshold, Nat. Photonics **11**, 289 (2017).
[111] A. Karnieli and S. Fan, Jaynes-Cummings interaction between low-energy free electrons and cavity photons, Sci. Adv. **9**, eadh2425 (2023).
[112] Raphael Dahan, Saar Nehemia, Michael Shentcis, Ori Reinhardt, Yuval Adiv, Xihang Shi, Orr Be'er, Morgan H. Lynch, Yaniv Kurman, Kangpeng Wang, and Ido Kaminer, Resonant phase-matching between a light wave and a free-electron wavefunction, Nat. Phys. **16**, 1123 (2020).
[113] Marco Turchetti, Chung-Soo Kim, Richard Hobbs, Yujia Yang, Pieter Kruit, and Karl K. Berggren, Design and simulation of a linear electron cavity for quantum electron microscopy, Ultramicroscopy **199**, 50 (2019).
[114] M. A. R. Krielaart and P. Kruit, Flat electron mirror, Ultramicroscopy **220**, 113157 (2021).
[115] Jo Verbeeck, Armand Béché, Knut Müller-Caspary, Giulio Guzzinati, Minh Anh Luong, and Martien Den Hertog, Demonstration of a 2×2 programmable phase plate for electrons, Ultramicroscopy **190**, 58 (2018).
[116] S. V. Yalunin, A. Feist, and C. Ropers, Tailored high-contrast attosecond electron pulses for coherent excitation and scattering, Phys. Rev. Res. **3**, L032036 (2021).
[117] O. Reinhardt and I. Kaminer, Theory of shaping electron wavepackets with light, ACS Photonics **7**, 2859 (2020).
[118] G. Baranes, R. Ruimy, A. Gorlach, and I. Kaminer, Free electrons can induce entanglement between photons, npj Quantum Inf. **8**, 1 (2022).
[119] R. Zimmermann, M. Seidling, and P. Hommelhoff, Charged particle guiding and beam splitting with autoponderomotive potentials on a chip, Nat. Commun. **12**, 1 (2021).
[120] D. L. Freimund, K. Aflatooni, and H. Batelaan, Observation of the Kapitza–Dirac effect, Nature **413**, 142 (2001).
[121] Malo Bézard, Imène Si Hadj Mohand, Luigi Ruggierio, Arthur Le Roux, Yves Auad, Paul Baroux, Luiz H. G. Tizei, Xavier Chécoury, and Mathieu Kociak, High efficiency coupling of free electrons to sub-λ3 modal volume, high-Q photonic cavities, arXiv:2307.15556 (2023).
[122] Yannick D'Mello, Raphael Dahan, Santiago Bernal, Xihang Shi, Ido Kaminer, and David V. Plant, Efficient coupling between free electrons and the supermode of a silicon slot waveguide, Opt. Express **31**, 19443 (2023).
[123] E. Peter, P. Senellart, D. Martrou, A. Lemaître, J. Hours, J. M. Gérard, and J. Bloch, Exciton-photon strong-coupling regime for a single quantum dot embedded in a microcavity, Phys. Rev. Lett. **95**, 067401 (2005).
[124] Dror Liran, Jiaqi Hu, Nathanial Lydick, Hui Deng, Loren Pfeiffer, Ronen Rapaport, Electrically controlled dipolariton circuits, arXiv:2308.08289 (2023).
[125] J. R. Guest, T. H. Stievater, Xiaoqin Li, Jun Cheng, D. G. Steel, D. Gammon, D. S. Katzer, D. Park, C. Ell, A. Thränhardt, G. Khitrova, and H. M. Gibbs, Measurement of optical absorption by a single quantum dot exciton, Phys. Rev. B **65**, 241310 (2002).
[126] T. H. Stievater, Xiaoqin Li, D. G. Steel, D. Gammon, D. S. Katzer, D. Park, C. Piermarocchi, and L. J. Sham, Rabi oscillations of excitons in single quantum dots, Phys. Rev. Lett. **87**, 133603 (2001).
[127] G. Khitrova, H. M. Gibbs, M. Kira, S. W. Koch, and A. Scherer, Vacuum Rabi splitting in semiconductors, Nat. Phys. **2**, 81 (2006).
[128] Shuren Hu, Marwan Khater, Rafael Salas-Montiel, Ernst Kratschmer, Sebastian Engelmann, William M. J. Green, and Sharon M. Weiss, Experimental realization of deep-subwavelength confinement in dielectric optical resonators, Sci. Adv. **4**, eaat2355 (2018).
[129] R. Shiloh, T. Chlouba, and P. Hommelhoff, Quantum-coherent light-electron interaction in an SEM, Phys. Rev. Lett. **128**, 235301 (2022).
[130] Xu Wang, Samantha Grist, Jonas Flueckiger, Nicolas A. F. Jaeger, and Lukas Chrostowski, Silicon photonic slot waveguide Bragg gratings and resonators, Opt. Express **21**, 19029 (2013).
[131] A. Fu, H. Gao, P. Petrov, and P. Yang, Widely tunable distributed Bragg reflectors integrated into nanowire waveguides, Nano Lett. **15**, 6909 (2015).
[132] Limin Tong, Jingyi Lou, and Eric Mazur, Single-mode guiding properties of subwavelength-diameter silica and silicon wire waveguides, Opt. Express **12**, 1025 (2004).
[133] Yi Yang, Charles Roques-Carmes, Steven E. Kooi, Haoning Tang, Justin Beroz, Eric Mazur, Ido Kaminer, John D. Joannopoulos, and Marin Soljačić, Photonic flatband resonances for free-electron radiation, Nature **613**, 42 (2023).
[134] X. Gao, B. Zhen, M. Soljačić, H. Chen, and C. W. Hsu, Bound states in the continuum in fiber Bragg gratings, ACS Photonics **6**, 2996 (2019).
[135] A. Blais, A. L. Grimsmo, S. M. Girvin, and A. Wallraff, Circuit quantum electrodynamics, Rev. Mod. Phys. **93**, 025005 (2021).
[136] J. Bourassa, F. Beaudoin, J. M. Gambetta, and A. Blais, Josephson-junction-embedded transmission-line resonators: From Kerr medium to in-line transmon, Phys. Rev. A **86**, 013814 (2012).
[137] Fumiki Yoshihara, Tomoko Fuse, Sahel Ashhab, Kosuke Kakuyanagi, Shiro Saito, and Kouichi Semba, Superconducting qubit–oscillator circuit beyond the ultrastrong-coupling regime, Nat. Phys. **13**, 44 (2016).
[138] P. Alsing, D. S. Guo, and H. J. Carmichael, Dynamic Stark effect for the Jaynes-Cummings system, Phys. Rev. A **45**, 5135 (1992).
[139] D. P. DiVincenzo, The physical implementation of quantum computation, Fortschr. Phys. **48**, 771 (2000).

[140] A. Y. Kitaev, Fault-tolerant quantum computation by anyons, Ann. Phys. (N. Y). **303**, 2 (2003).
[141] R. Raussendorf, J. Harrington, and K. Goyal, A fault-tolerant one-way quantum computer, Ann. Phys. (N. Y). **321**, 2242 (2006).
[142] K. Kieling, T. Rudolph, and J. Eisert, Percolation, renormalization, and quantum computing with nondeterministic gates, Phys. Rev. Lett. **99**, 130501 (2007).
[143] M. Brune, F. Schmidt-Kaler, A. Maali, J. Dreyer, E. Hagley, J. M. Raimond, and S. Haroche, Quantum Rabi oscillation: A direct test of field quantization in a cavity, Phys. Rev. Lett. **76**, 1800 (1996).
[144] Barak Dayan, A. S. Parkins, Takao Aoki, E. P. Ostby, K. J. Vahala, and H. J. Kimble, A photon turnstile dynamically regulated by one atom, Science **319**, 1062 (2008).
[145] P. J. Bardroff, E. Mayr, and W. P. Schleich, Quantum state endoscopy: Measurement of the quantum state in a cavity, Phys. Rev. A **51**, 4963 (1995).
[146] P. Walther, K. J. Resch, T. Rudolph, E. Schenck, H. Weinfurter, V. Vedral, M. Aspelmeyer, and A. Zeilinger, Experimental one-way quantum computing, Nature **434**, 169 (2005).
[147] T. Rudolph, Why I am optimistic about the silicon-photonic route to quantum computing, APL Photonics **2**, 030901 (2017).
[148] J. Hastrup and U. L. Andersen, Protocol for generating optical Gottesman-Kitaev-Preskill states with cavity QED, Phys. Rev. Lett. **128**, 170503 (2022).
[149] Gefen Baranes, Shiran Even-Haim, Ron Ruimy, Alexey Gorlach, Raphael Dahan, Asaf A. Diringer, Shay Hacohen-Gourgy, and Ido Kaminer, Free-electron interactions with photonic GKP states: Universal control and quantum error correction, Phys. Rev. Res. **5**, 043271 (2023).
[150] J. Kerckhoff, H. I. Nurdin, D. S. Pavlichin, and H. Mabuchi, Designing quantum memories with embedded control: Photonic circuits for autonomous quantum error correction, Phys. Rev. Lett. **105**, 040502 (2010).
[151] S. Trotzky, P. Cheinet, S. Fölling, M. Feld, U. Schnorrberger, A. M. Rey, A. Polkovnikov, E. A. Demler, M. D. Lukin, and I. Bloch, Time-resolved observation and control of superexchange interactions with ultracold atoms in optical lattices, Science **319**, 295 (2008).
[152] A. Karnieli, N. Rivera, A. Arie, and I. Kaminer, The coherence of light is fundamentally tied to the quantum coherence of the emitting particle, Sci. Adv. **7**, eabf8096 (2021).
[153] A. Karnieli, N. Rivera, A. Arie, and I. Kaminer, Superradiance and subradiance due to quantum interference of entangled free electrons, Phys. Rev. Lett. **127**, 060403 (2021).
[154] D. Manzano, A short introduction to the Lindblad master equation, AIP Adv. **10**, 025106 (2020).
[155] R. W. Boyd, *Nonlinear Optics* (Academic Press, Cambridge, MA, USA, 2008).
[156] W. P. Putnam, and O. E. Ates, Subwavelength-modulated waveguides for phase-matching photons and low-energy electrons. CLEO 2023 (2023), Pap. FW3C.6 FW3C.6 (2023). https://doi.org/10.1364/CLEO_FS.2023.FW3C.6.